Title: Diagnosing seasonal to multi-decadal phytoplankton group dynamics in a highly productive coastal ecosystem

Authors: D. Catlett[1]*, D. A. Siegel[1,2], R. D. Simons[1], N. Guillocheau[1], F. Henderikx-Freitas[3], C. S. Thomas[4]

[1]Earth Research Institute, UC Santa Barbara, Santa Barbara, CA, USA

[2]Department of Geography, UC Santa Barbara, Santa Barbara, CA, USA

[3]Department of Oceanography, University of Hawai‘i at Manoa, Honolulu, HI, USA

[4]Ocean Ecology Laboratory, NASA Goddard Space Flight Center, Greenbelt, MD, USA

*Correspondence: dsc@ucsb.edu

Highlights

- Bio-optical models extend an HPLC phytoplankton pigment data set to two decades
- Seasonal to decadal dynamics in 5 phytoplankton biomarker pigments are quantified
- Oceanographic and climate forcings of biomarker pigment dynamics are assessed
- Decadal dinoflagellate blooms are associated with the NPGO and anomalous advection
- Some small phytoplankton groups respond positively to seasonal upwelling

Keywords

Phytoplankton, community composition, climate, upwelling, bio-optics

Abstract

The Santa Barbara Channel, CA (SBC) is a biodiverse marine ecosystem fueled largely by phytoplankton productivity, and the composition of the phytoplankton community influences the magnitude and fates of this productivity. Here, we create a 22-year monthly time series of phytoplankton biomarker pigment concentrations in the SBC by combining 12 years of high performance liquid chromatography phytoplankton pigment concentrations with bio-optical models and 10 additional years of bio-optical observations. The bio-optical models skillfully predict biomarker pigment concentrations representative of five distinct phytoplankton groups (PGs; diatoms, dinoflagellates, chlorophytes, prymnesiophytes, and picophytoplankton) and resolve seasonal responses to the annual upwelling-relaxation cycle for all PGs except the dinoflagellates. Our observations indicate that nanophytoplankton groups respond most rapidly to seasonal upwelling, followed by diatoms, and then by picophytoplankton as the water column stratifies in the summer. A Regional Ocean Modeling System (ROMS) solution is used to relate advection of different source waters to the observed PG dynamics. The ROMS simulation results suggest that, on seasonal time scales, pronounced cross-SBC differences in PG seasonality are related to cross-SBC differences in source waters. El Niño Southern Oscillation events drive interannual variability in the upwelling response of most PGs. On decadal time scales, dinoflagellate blooms are associated with the warm phase of the North Pacific Gyre Oscillation and anomalous advection of Southern California Bight source waters into the SBC. Taken together, our results provide a novel view of phytoplankton community succession in response to seasonal upwelling by considering the dynamics of pico- and nano-phytoplankton and suggest that regional surface ocean advection plays a substantial role in driving phytoplankton composition in the SBC.

1. Introduction

The Santa Barbara Channel, CA (SBC, Figure 1) is an exceptionally productive, biodiverse, and well-studied coastal marine ecosystem at the boundary of the relatively cool, productive California Current System (CCS) and the warmer, more oligotrophic Southern California Bight (SCBight) (Beers, 1986; Harms and Winant, 1998; Venrick, 1998; Brzezinski and Washburn, 2011; Henderikx Freitas et al., 2017). Pronounced spatiotemporal gradients in oceanographic features are frequently observed in the SBC due to its location in the "transition zone" between the CCS and SCBight, and phytoplankton blooms are often more intense in the SBC relative to the surrounding region (Harms and Winant, 1998; Venrick, 1998; Brzezinski and Washburn, 2011; Henderikx Freitas et al., 2017). Variations in phytoplankton community composition in the SBC are also dynamic, though under-explored, and are known to impact pelagic food webs and elemental cycling throughout coastal California and the world's oceans (Beers, 1986; Field et al., 1998; Guidi et al., 2016; Lin et al., 2017).

Large spatiotemporal variations in oceanographic properties are often observed in the SBC and result from regional atmospheric and oceanic circulation patterns associated with the annual upwelling-relaxation cycle in combination with the unique geometry of the SBC coastline (Harms and Winant, 1998; Winant et al., 2003; Brzezinski and Washburn, 2011). Point Conception roughly marks the northwest corner of the SBC. Here, the orientation of the California coastline and coastal mountain ranges shifts from north-south to east-west. This shift creates an upwelling shadow where upwelling winds are strongest on the west side of the SBC near Point Conception and progressively weaken towards the eastern SBC (Harms and Winant, 1998; Winant et al., 2003; Fewings et al., 2015). Over the course of an annual cycle, wind-driven upwelling is strongest during the spring and early summer and to the north and west of the SBC

in the southern CCS. Upwelling introduces nutrients to the euphotic zone and allows for the accumulation of phytoplankton, most notably diatoms, in the surface ocean (McPhee-Shaw et al., 2007; Brzezinski and Washburn, 2011; Krause et al., 2013). The persistent wind-driven equatorward flows of the CCS maintain a pressure gradient that drives the poleward flowing California Countercurrent in the nearshore waters off Southern California as well as larger-scale poleward flows at the onset of wind relaxations (Harms and Winant, 1998; Winant et al., 2003; Melton et al., 2009). These circulation patterns result in the entrainment of cold, productive, nutrient-rich waters into the southwestern SBC, and warmer, more oligotrophic waters into the northeastern SBC. While the relative strength of these two circulation patterns can vary on daily to seasonal or longer time scales, the combination of these flows leads to the persistence of a convergent, cyclonic eddy that can further concentrate particles and primary productivity in the central SBC (Harms and Winant, 1998; Brzezinski and Washburn, 2011; Simons et al., 2015). On smaller spatiotemporal scales and in particular on the inner continental shelf, a complex combination of local wind-driven upwelling, internal wave and tide dynamics, freshwater discharge events, and surface gravity waves can significantly influence primary productivity and particle loads in the SBC (Warrick et al., 2004; McPhee-Shaw et al., 2007; Lucas et al., 2011; Henderikx Freitas et al., 2017).

Interannual variations in the physical and biological oceanography of the SBC and surrounding waters are primarily modulated by natural climate oscillations including the El Niño Southern Oscillation (ENSO) (Bograd and Lynn, 2001; Chavez et al., 2002; Venrick, 2012; Jacox et al., 2016), the Pacific Decadal Oscillation (PDO) (Mantua et al., 1997; Chhak and Di Lorenzo, 2007; Di Lorenzo et al., 2013), and the North Pacific Gyre Oscillation (NPGO) (Di Lorenzo et al., 2008; Di Lorenzo et al., 2013). The ENSO exhibits a 3- to 5-year periodicity and

has long been recognized as a prominent driver of interannual variations in biological responses to seasonal upwelling in the SBC and surrounding waters. During extreme El Niño events, upwelling winds are suppressed, the water column is anomalously stratified, and warm sea surface temperatures and low phytoplankton biomass are often observed (Bograd and Lynn, 2001; Shipe et al., 2002; Jacox et al., 2014; Jacox et al., 2016). Conversely, La Niña conditions signify an enhancement of seasonal upwelling and a relatively shallow nutricline (Venrick, 2012; Jacox et al., 2016). Several recent studies have demonstrated the role of two dominant modes of North Pacific decadal climate variability, the PDO and NPGO, in driving oceanographic variability in the CCS and SCBight. The PDO is thought to exert a stronger impact on the northern CCS above ~38° N (Di Lorenzo et al., 2008; Di Lorenzo et al., 2013), while the NPGO is associated with low-frequency oscillations in salinity, nutrient concentrations, and phytoplankton biomass in the southern CCS and SCBight (Di Lorenzo et al., 2008; Di Lorenzo et al., 2013). The cold phase of the NPGO (PDO), signified by positive (negative) values of the corresponding statistical index, indicates stronger wind-driven upwelling and enhanced equatorward flows in the southern (northern) CCS, while the warm phase of the NPGO (PDO) is associated with a relaxation and postponement of seasonal upwelling and enhanced poleward flows in the CCS (Mantua et al., 1997; Di Lorenzo et al., 2008; Di Lorenzo et al., 2013).

Like the physical forcings in the region, phytoplankton communities of the SBC and surrounding waters have been studied for many years and are highly variable across a range of temporal and spatial scales (Allen, 1942; Reid et al., 1978; Goodman et al., 1984; Venrick, 2002; Anderson et al., 2008; Goodman et al., 2012; Venrick, 2012; Taylor et al., 2015; Needham and Fuhrman, 2016). Cell abundances of a given species can vary by orders of magnitude on time scales of days to weeks (Goodman et al., 1984; Bialonski et al., 2016; Barth et al., 2020) and on

spatial scales less than one km (Reid et al., 1978; Goodman et al., 2012), and the dominant species within a bloom sampled at a fixed point in space can change daily (Needham and Fuhrman, 2016). Generally, dinoflagellates, prymnesiophytes, and picophytoplankton dominate the phytoplankton community under stratified, low biomass conditions, and in offshore waters of the SCBight and CCS regions (Venrick, 2002; Taylor et al., 2015). Diatoms have repeatedly been shown to dominate cell abundances, carbon biomass, and phytoplankton pigment distributions in the SBC and CCS to the north and west (Venrick, 2002; Anderson et al., 2006; Anderson et al., 2008; Venrick, 2012; Taylor et al., 2015). Along the continental shelf of the SBC and CCS, and more prominently in the SCBight, "red tide" dinoflagellate blooms are frequently observed (Allen, 1942; Gregorio and Pieper, 2000; Barth et al., 2020; Fischer et al., 2020), with longer periods of elevated dinoflagellate abundances observed about once every decade since the early 1900s (Gregorio and Pieper, 2000; Smayda and Trainer, 2010; Fischer et al., 2020). Picoeukaryote blooms dominated by small (< 2 µm) chlorophytes such as *Ostreococcus*, in addition to blooms of the cyanobacterium *Synechococcus*, have been documented in the nearshore waters of the SCBight, but have yet to be observed in the SBC (Palenik, 2000; Worden et al., 2004; Countway and Caron, 2006). Finally, blooms of the prymnesiophytes *Phaeocystis sp.* and *Emiliania huxleyi* have been documented in the SBC (Goodman et al., 2012; Wear et al., 2015; Matson et al., 2019), although such observations are less common and, in the case of the recent *E. huxleyi* bloom documented in Matson et al. (2019), unprecedented.

High performance liquid chromatography (HPLC) analysis of phytoplankton pigment concentrations is widely used to assess phytoplankton group (PG) variations (Vidussi et al., 2001; Uitz et al., 2006; Anderson et al., 2008; Kramer and Siegel, 2018). The HPLC method

measures the concentrations of ~25 phytoplankton pigments, some of which can be used as "biomarkers" for particular PGs. The benefits of HPLC pigment analysis are the rigorously quality-controlled and standardized analytical procedures (Van Heukelem and Thomas, 2001; Hooker et al., 2010), and the direct links between biomarker pigment concentrations and bio-optical properties that allow for predictions of pigment concentrations from bio-optical observations (Chase et al., 2017; Catlett and Siegel, 2018). As with all methods currently used to quantify phytoplankton community composition, HPLC pigment analysis has limitations and uncertainties; these include ambiguity in the taxonomic identities of many commonly used biomarker pigments, and the complex and variable relationships between biomarker pigment concentrations and cell abundances, carbon biomass, and primary production (Higgins et al., 2011; Jeffrey et al., 2011). Nonetheless, recent work shows that the concentrations of several important biomarker pigments can be modeled from bio-optical observations with high fidelity in the SBC (Catlett and Siegel, 2018), providing an opportunity to create a multi-decadal biomarker pigment data record for this site. Such large-scale investigations of PG dynamics are of utmost importance as the impacts of climate forcings on PG variations remain poorly understood.

Here, we create an approximately monthly 22-year time series of phytoplankton biomarker pigment concentrations by merging recently developed bio-optical models and 22 years of bio-optical observations with 12 years of HPLC phytoplankton pigment measurements. This time series is used to quantify seasonal to multi-decadal PG variations in the SBC and investigate associations of PGs with oceanographic and climate forcings. Our results demonstrate the dominance of the seasonal upwelling cycle in driving variations of most PGs in the SBC. Using a high-resolution Regional Ocean Modeling System (ROMS) solution, we present evidence that, on seasonal time scales, cross-SBC variability in source waters is linked to spatial

variability in PG seasonal cycles. On interannual to decadal time scales, most PGs are impacted by El Niño Southern Oscillation events. Conversely, anomalous decadal dinoflagellate blooms are associated with the warm phase of the North Pacific Gyre Oscillation and anomalous advection of SCBight source waters. This study demonstrates the successful application of a bio-optical model to extend a PG biomarker pigment time series and furthers our understanding of the coupling amongst seasonal upwelling, natural climate oscillations, and advection in driving seasonal to multi-decadal PG variations in the SBC.

2. Methods

2.1. Plumes and Blooms Overview

Plumes and Blooms (PnB) has sampled 7 stations approximately monthly on a South-to-North transect in the SBC (Figure 1) since August, 1996 (Otero and Siegel, 2004). Station 7, usually the first station sampled on each PnB cruise, is the Southern-most station and is located on the continental shelf of the Channel Islands in ~75 m of water, while Station 1 is the Northern-most station located on the mainland continental shelf with a water depth of ~45 m (Figure 1). All other PnB stations lie at water depths greater than 200 m. A graphical representation of the coverage of the biomarker pigment data set is shown in Supporting Figure S1. January and February are under-sampled by PnB due to annual ship maintenance, and Station 7 is under-sampled relative to the other PnB stations due to harsher conditions at sea. Multiple PnB cruises were occasionally conducted in the same month, particularly in the first half of the time series. Significant (> 2 months) gaps in the merged biomarker pigment time series (see Section 2.7) occurred from August-October, 2006, March-June, 2010, and July-September, 2018 (Supp. Figure S1).

Due to previously documented analytical issues (Hooker et al., 2010; Barrón et al., 2014), PnB HPLC pigment observations are considered here from November, 2005 to November, 2018 (the same data set considered in Catlett and Siegel, 2018, with the addition of observations from 2015-2018). Bio-optically modeled pigment observations rely on the phytoplankton absorption coefficient ($a_{ph}(\lambda)$), available from April, 1997 to June, 2018. Other PnB data products including potential temperature, salinity, fluorometric chlorophyll *a* concentrations (CHL; see Table 1), and macronutrient concentrations are considered from April, 1997 to November, 2018.

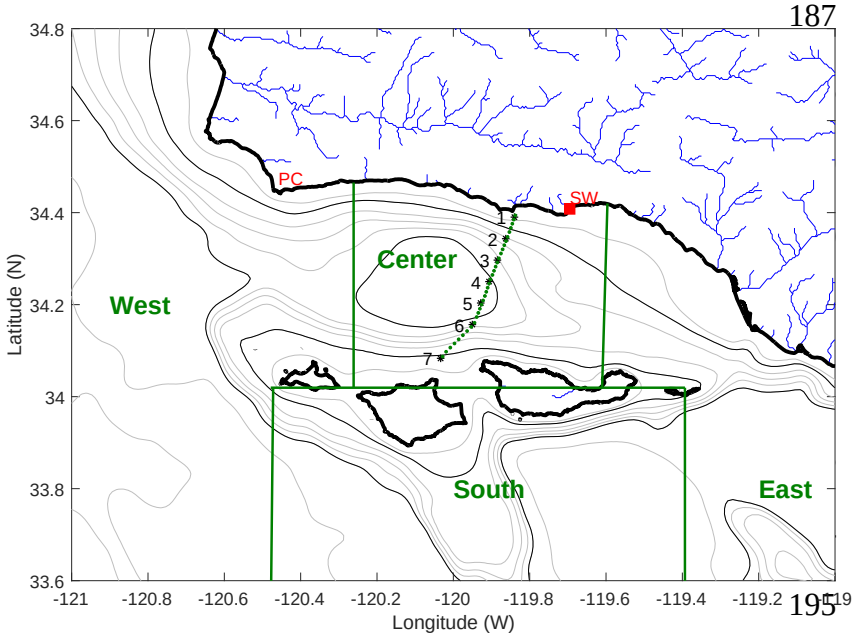

Figure 1. Map of the Santa Barbara Channel, CA. Plumes and Blooms stations are marked with black stars and labeled with station numbers. Bold black lines indicate coastline. Gray bathymetry contours are shown at 50, 200, 300, 400, 1000, 2000, 3000, and 4000 m water depth. Black bathymetry contours are the 100 and 500 m isobaths. Particle release points used in the ROMS particle tracking model are shown with green circles, and the four "origin boxes" (West, Center, East, South) used to define Santa Barbara Channel source waters are outlined with bold green lines (see Sections 2.8.2 and 4.3). The red square indicates Stearns Wharf (SW) where weekly microscopic counts of several phytoplankton species are performed (see Section 2.8.3). Point Conception (PC) is noted in red.

2.2. Plumes and Blooms Oceanographic Observations

To determine associations of PGs with oceanographic processes, we consider potential temperature (henceforth referred to as temperature) and salinity profiles, as well as CHL and

dissolved inorganic nutrient concentrations (nitrate, phosphate, and silicate) determined from discrete seawater samples. For most CTD profiles, a Sea-Bird Electronics 911E CTD was deployed on a SBE32C compact carousel. However, from December 2000 to March 2003, a Sea-Bird Electronics SeaCat Profiler CTD was used instead. CTD profiles are considered over the upper 100 m of the water column and are binned to 1 m depth intervals. To quality control the CTD profiles, spurious values of temperature and salinity (temperature > 25 ºC; salinity < 32 psu or > 34.5 psu) were removed and profiles were de-spiked as recommended by the United States Integrated Ocean Observing System (2013). Following de-spiking, 16 temperature and 32 salinity profiles with missing data for > 25% of the depths sampled were discarded.

Discrete seawater samples were collected from 5 L Niskin bottles for analysis of bulk chlorophyll *a* and dissolved inorganic nutrient concentrations. For analysis of chlorophyll *a* concentrations, particles were collected on Whatman GF/F filters via vacuum filtration and immediately frozen and stored in liquid nitrogen. Filters were extracted in 90% acetone overnight and analyzed on a Turner Designs 10AU fluorometer before and after the addition of 2 drops of 1.2 M HCl to determine chlorophyll *a* and phaeopigment concentrations. Samples for dissolved inorganic nutrient concentrations were collected in 20 mL plastic scintillation vials and frozen until analysis with flow injection techniques at the UCSB Marine Science Institute Analytical Lab (Johnson et al., 1985). The detection limits are 0.1 μM for nitrite, 0.2 μM for nitrate plus nitrite, 0.05 μM for ortho-phosphate, and 0.2 μM for silicate (http://msi.ucsb.edu/services/analytical-lab/seawater-nutrients-fia). Nitrate concentrations are determined by subtracting nitrite concentrations from the total concentration of nitrite and nitrate. Values below detection for phosphate and silicate were set to 0 μM. Where nitrate plus nitrite concentrations were below detection, nitrate values were set to 0 μM. All curated PnB

CTD and water sample data analyzed here are publicly available (Catlett et al., 2020a). In all analyses considered here, PnB oceanographic observations are considered from April, 1997 to November, 2018 to match the time period from which HPLC phytoplankton pigment observations are available (see section 2.7 below).

Table 1. Pigment abbreviations and biomarker assumptions used in the present study. The five representative biomarker pigments and their taxonomic representation were inferred from the results of the cluster analysis presented in Figure 2 and the literature (Vidussi et al., 2001; Uitz et al., 2006; Jeffrey et al., 2011). The color-coding of each biomarker pigment corresponds to that used in subsequent figures.

Pigment	Abbreviation	Assumed Taxonomic Significance
Total chlorophyll *a*	TChla[1]	All phytoplankton
Total chlorophyll *b*	TChlb	Chlorophytes
Alpha-beta-carotene	ABCar	-
19'-butanoyloxyfucoxanthin	But	-
19'-hexanoyloxyfucoxanthin	Hex	Prymnesiophytes
Alloxanthin	Allo	-
Diadinoxanthin	Diadino	-
Diatoxanthin	Diato	-
Fucoxanthin	Fuco	Diatoms
Peridinin	Perid	Dinoflagellates
Zeaxanthin	Zea	Picophytoplankton
Divinyl chlorophyll *a*	DVChla	-
Chlorophyll c1 + c2	Chlc1c2	-
Chlorophyll c3	Chlc3	-
Lutein	Lut	-
Neoxanthin	Neo	-
Violaxanthin	Viola	-
Prasinoxanthin	Pras	-

[1]TChla is used to indicate total chlorophyll *a* concentrations determined by HPLC. Because the bio-optical models are trained on HPLC data, TChla also includes bio-optically modeled concentrations of total chlorophyll *a*. CHL is used to denote chlorophyll *a* concentrations determined by fluorometric methods (see Section 2.2).

2.3. HPLC Methods and Data-Driven PG Determinations

Discrete seawater samples for HPLC analysis of phytoplankton pigment concentrations were collected from 5 L Niskin bottles deployed on a rosette and immediately concentrated on GF/F filters by vacuum filtration. Filters were flash-frozen in liquid nitrogen, and stored in liquid

nitrogen or at -80°C until HPLC analysis using the method of Van Heukelem and Thomas, 2001. HPLC analysis was conducted at Horn Point Laboratory for all samples collected prior to March, 2011. After March 2011, HPLC analysis was carried out at the NASA Goddard Space Flight Center. Pigment concentrations below the limit of detection were assumed absent from the sample and their concentrations were set to zero. HPLC reporting practices varied over the course of the PnB record. Current practices report pigment concentrations to 0.001 μg L^{-1}. Thus, for data that were reported to four places after the decimal, values were rounded to the nearest thousandth to maintain consistency throughout the HPLC record. The pigments considered in the present analysis, along with their abbreviations and assumed taxonomic representation, are shown in Table 1.

Although the same HPLC method has been used throughout the PnB record, the limits of quantitation of the method have changed over time due in part to the change in laboratories in 2011 along with changes made to the HPLC slit and step detector settings (which affected analysis of PnB samples collected from February, 2014 to the present). These changes only impact pigments with concentrations that are frequently at, near, or below the limits of detection and quantitation, and can impact assessments of their changes over time. In the PnB data, these pigments include DVChla, Pras, divinyl chlorophyll *b*, and gyroxanthin diester (see Table 1 for a list of pigment names, abbreviations, and assumed taxonomic significance). Divinyl chlorophyll *b* and gyroxanthin diester were not detected in 92.5% and 100% of the PnB samples considered here, respectively, and were not considered in subsequent analysis. Inspection of the dynamics of Pras and DVChla through time (Supp. Figure S2) suggested that measurements of DVChla were reasonably consistent across the two time periods with only minor variations observed that were likely driven by natural variability in the phytoplankton community. However, Pras was detected

far more frequently and at higher concentrations after the change in laboratory (Supp. Figures S2 and S3), suggesting analytical artifacts potentially interfered with the measurement of Pras.

The change in HPLC slit and step detector settings for samples collected after February, 2014 improved the signal:noise ratio of the HPLC method by approximately 40%, and therefore is expected to result in more frequent detection of pigments typically present in low concentrations (DVChla and Pras) over the course of the time series. We directly investigated the effects that the change in HPLC detector settings might have on our interpretations of the dynamics of these two pigments by applying the same, higher limits of quantification measured prior to the change in detector settings, to all DVChla and Pras data collected from 2011 to the present. For each year in the PnB HPLC record (excluding 2005 and 2010 due to insufficient sampling frequency), we then calculated the fraction of PnB stations where Pras or DVChla were not detected (Supp. Figure S3). Very minor changes in the fraction of observations below detection were observed for DVChla with the modified limits of quantification, suggesting the detector change did not substantially impact detection of this pigment in the PnB HPLC data. However, applying the 2011 limits of quantification to all subsequent observations of Pras dramatically increased the fraction of observations where Pras was reported (Supp. Figure S3). Further, from 2009 to 2011 (coinciding with a change in laboratories), the fraction of observations where Pras was not reported decreased nearly two-fold from 76% in 2009 to 43% in 2011. Finally, including Pras in subsequent analyses used for determining PG indices significantly altered our results (Figure 2, Supp. Figure S4). Due to the potential for these results to be driven by analytical artifacts, we thus excluded Pras from further analysis.

To determine the dominant PGs in the PnB HPLC record, we performed hierarchical cluster analysis on the phytoplankton pigment concentration data set using the correlation distance and Ward's linkage method (Latasa and Bidigare, 1998; Catlett and Siegel, 2018; the latter citation is henceforth referred to as CS18). We considered a similar suite of pigments to that used in CS18, but excluded Pras, as well as TChla in order to derive PGs independently of chlorophyll biomass. Five distinct pigment clusters were identified, each of which represent unique PGs that were identical to those identified in CS18 (Figure 2). Based on the associations of widely used biomarker pigments (Vidussi et al., 2001; Uitz et al., 2006; Jeffrey et al., 2011; Kramer and Siegel, 2018) with each cluster, five representative pigments were selected for further analysis and assumed to represent diatoms (Fuco), dinoflagellates (Perid), chlorophytes (TChlb), prymnesiophytes (Hex), and picophytoplankton (Zea). The concentrations of these biomarker pigments are used as proxies for the pigment biomass of each of these phytoplankton groups (PGs) in the remainder of this paper.

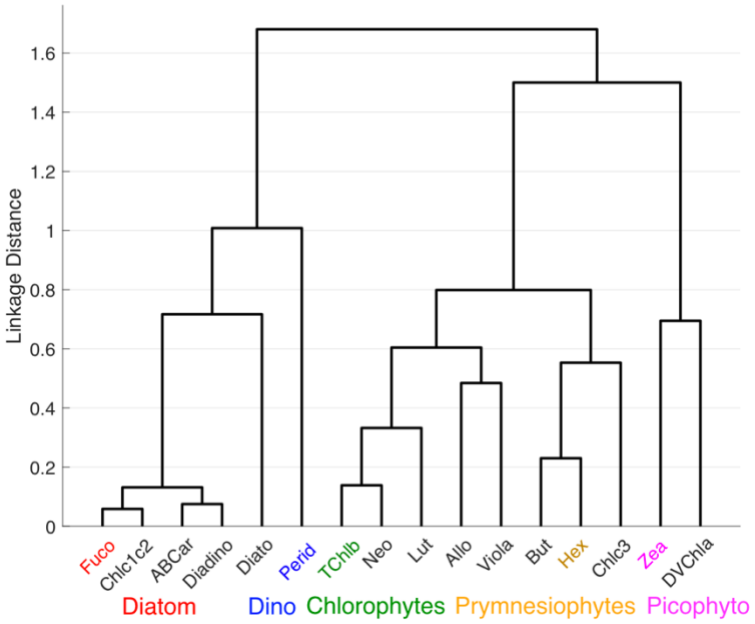

Figure 2. Hierarchical cluster analysis of HPLC phytoplankton pigment concentrations using the correlation distance and Ward's linkage method. Representative biomarker pigments and phytoplankton groups are color-coded here and in all subsequent analysis to aid interpretation.

2.4. Determinations of Spectrophotometric Absorption Coefficients

Discrete seawater samples were collected on PnB cruises for spectrophotometric determinations of the particulate absorption coefficient ($a_p(\lambda)$). These samples were filtered immediately using GF/Fs and stored in liquid nitrogen until analysis. $a_p(\lambda)$ was measured using the transmittance mode of the quantitative filter technique (Mitchell, 1990; Roesler et al., 2018) on a Perkin-Elmer Lambda 2 spectrophotometer equipped with a Labsphere RSA-PE-20 integrating sphere prior to April, 2003, and on a Shimadzu 2401-PC spectrophotometer equipped with an ISR-2200 integrating sphere from April, 2003 to the present. Following measurement of $a_p(\lambda)$, filters were extracted in methanol for 48 hours and the detrital absorption coefficient, $a_d(\lambda)$, was measured using a procedure identical to that used for $a_p(\lambda)$ on the extracted filter. The beta correction factor was determined empirically using natural phytoplankton communities from the SBC (Guillocheau, 2003). Phytoplankton absorption coefficients ($a_{ph}(\lambda)$) were derived by subtracting $a_d(\lambda)$ from $a_p(\lambda)$ and are considered here from 400-700 nm.

The Perkin-Elmer spectrophotometer occasionally introduced significant noise in estimates of $a_p(\lambda)$ (and by extension, $a_d(\lambda)$ and $a_{ph}(\lambda)$), particularly at shorter wavelengths (< 420 nm). Therefore, additional quality assurance and pre-processing procedures were employed to quality-control estimates of $a_{ph}(\lambda)$. First, the values of $a_d(400)/a_p(400)$ measured on the Perkin-Elmer were compared to the distribution of $a_d(400)/a_p(400)$ measured on the Shimadzu. Anomalously high values of $a_d(400)/a_p(400)$ were occasionally observed in data obtained with the Perkin-Elmer. Therefore, all three component spectra were discarded (104 total observations) when the Perkin-Elmer values were outside three standard deviations of the mean Shimadzu value. An additional 98 IOP determinations from both the Perkin-Elmer (77 observations) and Shimadzu (21 observations) spectrophotometers were discarded for various other reasons

(substantial baseline correction errors, highly aberrant spectral shapes, and signatures of incomplete pigment extractions in $a_d(\lambda)$).

2.5. Spectral derivative analysis and bio-optical modeling of biomarker pigments

Our goal is to assess patterns and forcings of phytoplankton biomarker pigment dynamics over the course of the 22-year PnB record. However, analytical issues preclude the use of PnB HPLC observations prior to November, 2005 (Barrón et al., 2014), and the integrity of nearly all HPLC samples from 2010 was compromised due to a dewar malfunction. PnB spectrophotometric IOP determinations are available for these time periods, providing a means to extend the time series of the five representative biomarker pigments (Fuco, Perid, TChlb, Hex, and Zea; Figure 2) and TChla to April, 1997. We thus employed a recently developed bio-optical modeling approach to extend the HPLC time series (CS18). The bio-optical modeling procedure utilizes the first and second derivatives of $a_{ph}(\lambda)$ ($a'_{ph}(\lambda)$ and $a''_{ph}(\lambda)$, respectively) to reliably model biomarker pigment concentrations (CS18). Following CS18, $a_{ph}(\lambda)$ spectral derivatives were calculated using a second order finite difference approximation after the application of a 15 nm Hamming window smoothing filter. Here, we considered values of $a_{ph}(\lambda)$ from 400-700 nm (and thus, spectral derivatives from 408-692 nm after application of the smoothing filter) due to inconsistent sampling of the 350-400 nm spectral range over the course of the PnB record.

Each pigment concentration, p_m, was then modeled as a linear sum of $a'_{ph}(\lambda)$ and $a''_{ph}(\lambda)$:

$$p_m = \sum_{i=1}^{N} A_m(\lambda_i) * a'_{ph}(\lambda_i) + B_m(\lambda_i) * a''_{ph}(\lambda_i) + C_m \quad (1)$$

where $a'_{ph}(\lambda)$ and $a''_{ph}(\lambda)$ are the first and second derivative, respectively, of smoothed $a_{ph}(\lambda)$, $A_m(\lambda)$ and $B_m(\lambda)$ are wavelength-specific coefficients, and $C_m(\lambda)$ is an arbitrary intercept. The empirical derivation of the wavelength-specific coefficients, $A_m(\lambda)$ and $B_m(\lambda)$, for each p_m is

described in detail in CS18. Briefly, 500-fold cross-validations of models for each pigment were performed using HPLC observations from November, 2005 to December, 2014 as in CS18. Thus, 500 unique models were developed for each pigment and the average goodness-of-fit statistics for these models are shown in Table 2 and Supporting Table S1. Overall, model performance was similar to that seen in CS18 and the 5 dominant biomarker pigments and TChla were consistently modeled with high fidelity in the cross-validation exercise. The concentrations of each of the five biomarker pigments were thus modeled at all PnB stations where $a_{ph}(\lambda)$ was available. Each p_m was modeled according to equation 1 using the ensemble mean of the 500 models (consisting of 500 $A_m(\lambda)$, $B_m(\lambda)$, $C_m(\lambda)$; see Supp. Figure S5 for mean +/- 95% confidence intervals of coefficients used for each p_m) determined during the 500-fold cross-validation. In order to maintain consistency with the HPLC data set, modeled pigment concentrations less than 0.0005 µg L^{-1} were replaced by 0 µg L^{-1}, and modeled concentrations greater than or equal to 0.0005 µg L^{-1} but less than 0.001 µg L^{-1} were rounded to 0.001 µg L^{-1}.

Table 2. Selected mean (standard deviation) goodness of fit statistics from the 500-fold model cross-validation procedure. See Supporting Table S1 for a more complete listing of goodness of fit statistics.

Pigment	R^2	Median % error
TChla	0.87 (0.07)	17.2 (2.18)
TChlb	0.86 (0.04)	21.7 (2.51)
Hex	0.72 (0.06)	29.8 (3.69)
Fuco	0.87 (0.07)	35.0 (4.93)
Perid	0.88 (0.05)	98.8 (3.68)
Zea	0.54 (0.09)	38.3 (3.72)

2.6. Additional independent model validations

The bio-optical models employed here may be particularly susceptible to two sources of uncertainty. First, the use of different spectrophotometers throughout the PnB record may bias the modeled pigment dynamics since different instruments introduce different degrees of noise

into spectral IOP measurements, which can then be accentuated by spectral derivative analysis. Second, the bio-optical models used here are formulated empirically, and so may be susceptible to overfitting to the training data. This may result in high uncertainties when the models are extrapolated to new time periods and environments.

To ensure pigment concentrations were modeled consistently across the different spectrophotometers, we compared fluorometric chlorophyll *a* concentrations (CHL) to TChla measured directly by HPLC ($TChla_{HPLC}$), modeled TChla derived from the Shimadzu 2401-PC $a_{ph}(\lambda)$ ($TChla_{Shim}$), and modeled TChla derived from the Perkin-Elmer Lambda 2 $a_{ph}(\lambda)$ ($TChla_{PE}$; Figure 3). CHL concentrations have been assessed using the same method throughout the PnB record. Monovinyl and divinyl chlorophyll *b* and chlorophyll *c* bias CHL determinations (Trees et al., 1985), so these comparisons are not expected to result in perfect agreement since the ratios of chlorophylls *b* and *c* to total chlorophyll *a* are not stable across samples. Nonetheless,

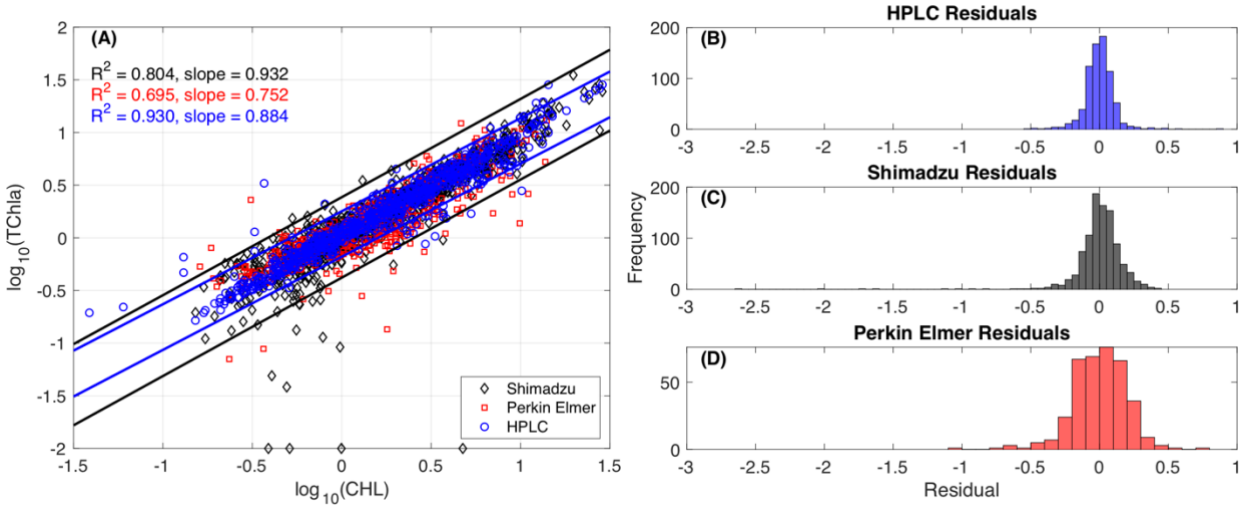

Figure 3. Regression (A) and residual (B, C, D) analysis of HPLC TChla concentrations (blue), TChla concentrations modeled from the Shimadzu 2401-PC $a_{ph}(\lambda)$ (black), and modeled TChla concentrations derived from the Perkin-Elmer Lambda 2 $a_{ph}(\lambda)$ (red) against fluorometric chlorophyll *a* concentrations (CHL). Blue and black lines in the scatterplot are 95% prediction intervals for the HPLC and Shimadzu TChla regressions, respectively. All residuals are log-transformed. 10^{-2} µg L^{-1} was added to all values to prevent undefined values in the log-transformed data.

comparing the three different indices of total chlorophyll *a* concentrations with CHL concentrations is expected to reveal any major biases in modeled pigment concentrations that may have been introduced by either spectrophotometer. As expected, all three chlorophyll *a* concentration metrics showed strong, statistically significant, linear relationships with CHL, with the strongest relationship observed for TChla$_{HPLC}$ (Figure 3A). The TChla residuals for all regression analyses were normally distributed and generally low in magnitude, with no obvious bias in any of the regression analyses (Figure 3B-D). While the slopes of all three regressions were significantly different from one another, most values of TChla$_{Shim}$ and TChla$_{PE}$ were within the 95% prediction intervals computed for the TChla$_{HPLC}$-CHL regression (Figure 3A). Taken together, these results suggest that the bio-optical models used here provide consistent estimates of chlorophyll *a* concentrations across the two spectrophotometers. We assume these results can be extrapolated to the modeled concentrations of the biomarker pigments considered here.

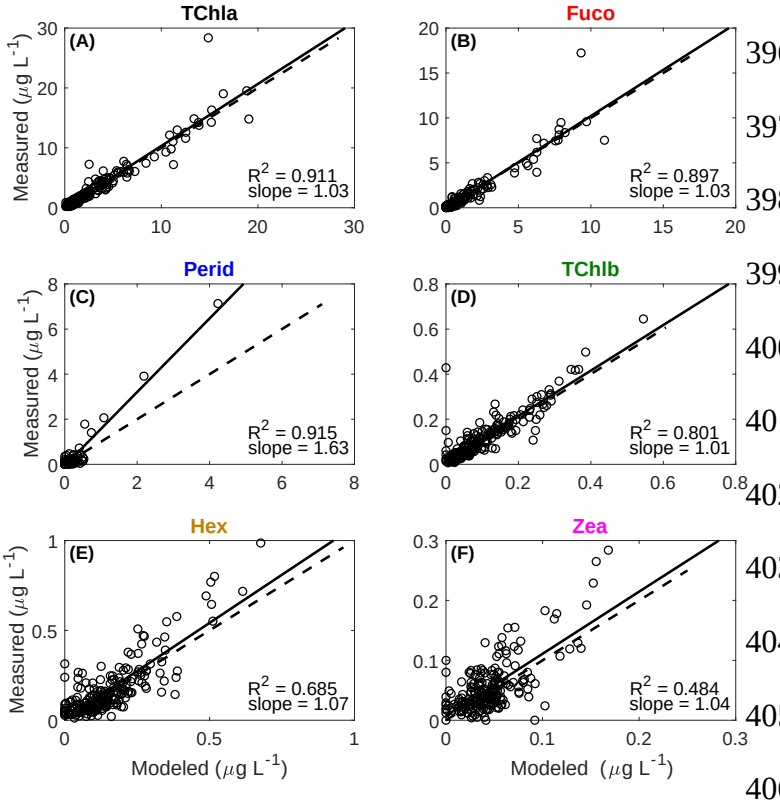

Figure 4. Validation of bio-optical models for (A) TChla, (B) Fuco, (C) Perid, (D) TChlb, (E) Hex, and (F) Zea extrapolated to HPLC observations not included in the model cross-validation exercise. Panel titles are color-coded as in Figure 2.

Additional independent model validations were performed to verify that the bio-optical models were not overfit to the training data used in the cross-validation exercise above. Since the cross-validations were performed with HPLC observations from 2005-2014, for this test we validated modeled concentrations of TChla and each of the five biomarker pigments against concurrent PnB HPLC observations from 2015 to 2018 (Figure 4). Model performance over this time period was excellent for the diatom and chlorophyte biomarkers ($R^2 > 0.8$, slope ~1; Figure 4B and 4D), with reasonable retrievals found for the prymnesiophyte biomarker ($R^2 > 0.7$, slope = 1.07; Figure 4E). While the model was able to reliably capture dinoflagellate "blooms" (Perid > ~0.5 µg L^{-1} was generally modeled as such; $R^2 = 0.91$), it consistently underestimated Perid concentrations when HPLC measured concentrations were high (slope > 1.5), and performed poorly when they were low (< ~0.3 µg L^{-1}; Figure 4C). Similar to the results of the cross-validation exercise, the model was able to explain ~50% of the variance in picoplankton pigment concentrations with minimal bias (slope = 1.04; Figure 4F). The reduced fidelity in modeled Zea concentrations is likely due to the low concentrations typically observed in the SBC relative to the other biomarker pigments, and its resulting small contributions to spectral absorption in this data set. Repeating this analysis with all available HPLC pigment observations from 2005-2018 (including the training data; Supp. Figure S6) and further inspection of the space-time distribution of residual errors over this time period (Supp. Figure S7) confirmed that the bio-optical models used here skillfully predict biomarker pigment concentrations across a wide range of oceanographic conditions and phytoplankton community states.

2.7. The "merged" pigment data set

All bio-optically modeled pigment concentrations lacking corresponding HPLC observations were merged with all HPLC observations to create a ~22-year, approximately monthly time series of TChla and the five major biomarker pigments at each of the seven PnB stations. Pigment concentrations from November, 2005 to November, 2018 were predominantly measured by HPLC. Pigment concentrations from April, 1997 to October, 2005, and from February to November of 2010 were estimated by the bio-optical models. The application of the bio-optical models extended the HPLC data set of 758 observations over 12 years to 1393 observations spanning roughly 22 years. This data set provides unprecedented spatiotemporal coverage of PG dynamics in the SBC. All phytoplankton pigment data presented here are publicly available (Catlett et al., 2020a).

2.8 Ancillary Data

We consider additional data beyond that available from PnB in the present analysis. These data include indices of the dominant modes of North Pacific climate variability, simulated surface ocean circulation patterns within and around the SBC, and microscopic counts of several species of diatoms and dinoflagellates at Stearns Wharf on the mainland shelf of the SBC.

2.8.1. Climate oscillation indices

Indices of climate oscillations used here include NOAA's Multivariate ENSO Index (MEI; https://psl.noaa.gov/enso/mei/) (Wolter and Timlin, 1993), the Southern Oscillation Index (SOI; https://www.ncdc.noaa.gov/teleconnections/enso/indicators/soi/data.csv), the Pacific Decadal Oscillation index (PDO; https://www.ncdc.noaa.gov/teleconnections/pdo/data.csv) (Mantua et al., 1997), and the North Pacific Gyre Oscillation index (NPGO;

http://www.o3d.org/npgo/npgo.php) (Di Lorenzo et al., 2008). El Niño conditions are indicated by positive (negative) values of the MEI (SOI), while the warm phase of the PDO (NPGO) is indicated by positive (negative) values. All climate indices are presented as provided by their maintainers and all include monthly values except for the MEI, where bimonthly means considering the preceding month's values are used (Wolter and Timlin, 1993).

2.8.2. Identifying PnB source waters with ocean circulation and particle tracking models

To determine the source waters of the PnB transect, a three-dimensional ocean circulation and Lagrangian particle tracking model was used. The ocean circulation model is a high-resolution Regional Ocean Modeling System (ROMS) solution for the SCBight region (Dong et al., 2009; Dong et al., 2017). The model domain is 674 km by 514 km with 1 km horizontal resolution and 42 vertical levels, and covers the California coast from Point Sur to the southern border with Mexico (Supp. Figure S8). The 1-km grid was nested from a larger 4-km grid that covers the U.S. West Coast (Dong et al., 2017). Our analyses are based on a 10-year ROMS hindcast solution for the years 2004 to 2013, which is stored as hourly offline solutions. As detailed in Dong et al (2017), the ROMS surface boundary conditions came from hourly Weather Research and Forecasting (WRF) products, and lateral boundary conditions from daily HYbrid Coordinate Ocean Model (HYCOM) global oceanic reanalysis products. The ROMS has been shown to accurately reproduce long-term means and seasonal and interannual variability of SCBight circulation (Dong et al., 2009, 2017) and resolve mesoscale features, such as eddies and upwelling, in the SBC (Dong et al., 2011; Simons et al., 2015).

The source waters of the PnB transect were identified using a Lagrangian particle tracking model driven by the ROMS-simulated flow fields (Carr et al., 2008; Simons et al.,

2013) and has been used extensively in the SBC and SCBight (Mitarai et al., 2009; Simons et al., 2015). Modeled particle trajectories have also shown good correspondence with surface drifter observations (Ohlmann and Mitarai, 2010). Using the offline ROMS flow fields, surface-following particles were projected backwards in time using the hourly ROMS output. In order to accurately capture the mesoscale circulation simulated by the ROMS, the PnB transect is represented by 34 particle release locations, approximately 1-km apart, that span PnB sample locations (Figure 1). Over the 10-year hindcast, particles were released daily from each of the 34 points along the PnB transect and tracked backwards in time along the water's surface for 15 days, for a total of 124,000 particles released and tracked over this time period.

We estimate the relative influence of SBC (local), SCBight, and southern CCS source waters on the PnB transect by computing the number of particles that originated from each of four "origin boxes" (West, Center, East, and South; see Figures 1 and 13). The origin box boundaries were selected based on qualitative evaluation of previous observations of surface ocean circulation and satellite observations of long-term mean sea-surface temperature (SST) and chlorophyll *a* concentrations in and around the SBC (Harms and Winant, 1998; Henderikx Freitas et al., 2017). The location of the lines demarcating the West, Center and East origin boxes were chosen such that the dominant circulation patterns would result in the transport of SCBight waters into the eastern entrance of the SBC and of southern CCS waters into the western entrance of the SBC on the advection time scales considered here. Particles originated from the South origin box only rarely, and are largely ignored here. The boundaries of the West and East origin boxes were also placed such that these two origin boxes would largely avoid the steepest east-west gradients in long-term average SST and chlorophyll *a* concentrations shown in Henderikx Freitas et al. (2017).

Daily time series of the number of particles originating from each origin box for each release point were constructed for 5-, 10- and 15-day advection times. Each daily time series was then binned by month. Monthly time series for individual PnB stations (Figure 1) were determined by binning the monthly time series of the four (for PnB station 1) or five (for PnB stations 2-7) closest release points to each PnB station, and another time series was created for the PnB transect by binning the monthly time series of all 34 release points. We consider the proportion of particles originating from the West, East, and Center origin boxes as proxies for the relative magnitude of advection of CCS, SCBight, and SBC source waters in each month of these time series, respectively. The proportion of particles originating from the South origin box was small (see Section 4.3 below), so these source waters are largely ignored in our discussion of these results. In section 4.3 we focus our discussion on results from 10-day hindcasts; qualitatively similar patterns (with expected differences in magnitudes of the proportion of particles from each origin box) were observed for 5- and 15-day advection times and those results are shown in Supporting Figures S9 and S10.

2.8.3. Additional phytoplankton group observations

To aid our discussion of seasonal succession in SBC PGs (see Section 4.4. and Supp. Figure S12 below), we consider observations of the abundances of several prominent diatom and dinoflagellate species at Stearns Wharf on the mainland shelf of the SBC. The Southern California Coastal Ocean Observing System (SCCOOS) Harmful Algal Bloom Monitoring Program provides observations of the abundances of several phytoplankton species (*Akashiwo sanguinea*, *Alexandrium sp.*, *Dinophysis sp.*, *Lingulodinium polyedra*, *Prorocentrum sp.*, *Ceratium sp.*, and *Cochlodinium sp*, *Pseudo-nitzschia sp.*) via the National Oceanic and

Atmospheric Administration's ERDDAP data portal (https://erddap.sccoos.org/erddap/tabledap/HABs-StearnsWharf.html). Phytoplankton species abundances are determined via microscopic identification and enumeration and are available approximately weekly. These data were retrieved on July 6, 2020 and are considered here from June 30, 2008 to February 10, 2020. Seasonal cycles for total dinoflagellates and for *Pseudo-nitzschia sp.* were computed from monthly mean time series of log-transformed weekly species counts. One cell mL^{-1} was added to both *Pseudo-nitzschia sp.* and total dinoflagellate counts to prevent undefined log-transformed values.

3. Results

3.1. Overview of SBC PG Dynamics

Table 3. Summary statistics of the merged biomarker pigment data set. All stations are considered independently. Max, maximum; CV, coefficient of variation (standard deviation divided by the mean); r, Pearson's correlation coefficient. Insignificant correlations at 95% confidence are not shown.

Pigment	Mean µg L^{-1}	Median µg L^{-1}	Max µg L^{-1}	CV (%)	r, TChlb	r, Hex	r, Fuco	r, Perid	r, Zea
TChla	2.57	1.53	35.0	122	0.27	0.09	0.95	0.28	
TChlb	0.11	0.08	0.65	84.9		0.65	0.12	0.19	0.51
Hex	0.15	0.12	1.13	80.4				0.10	0.36
Fuco	0.95	0.41	19.2	172					-0.07
Perid	0.16	0.05	7.13	264					0.10
Zea	0.05	0.04	0.28	71.4					

Each of the five PG biomarker pigment concentrations displayed unique spatiotemporal dynamics over the course of the 22 year time series (Figure 5). The diatom biomarker pigment, Fuco, was found at higher overall concentrations than the other four biomarker pigments (Table 3), and largely mirrored the TChla patterns (Table 3, Figure 5A and 5B). While Perid was most often found at much lower concentrations than the diatom biomarker pigment, and comparable

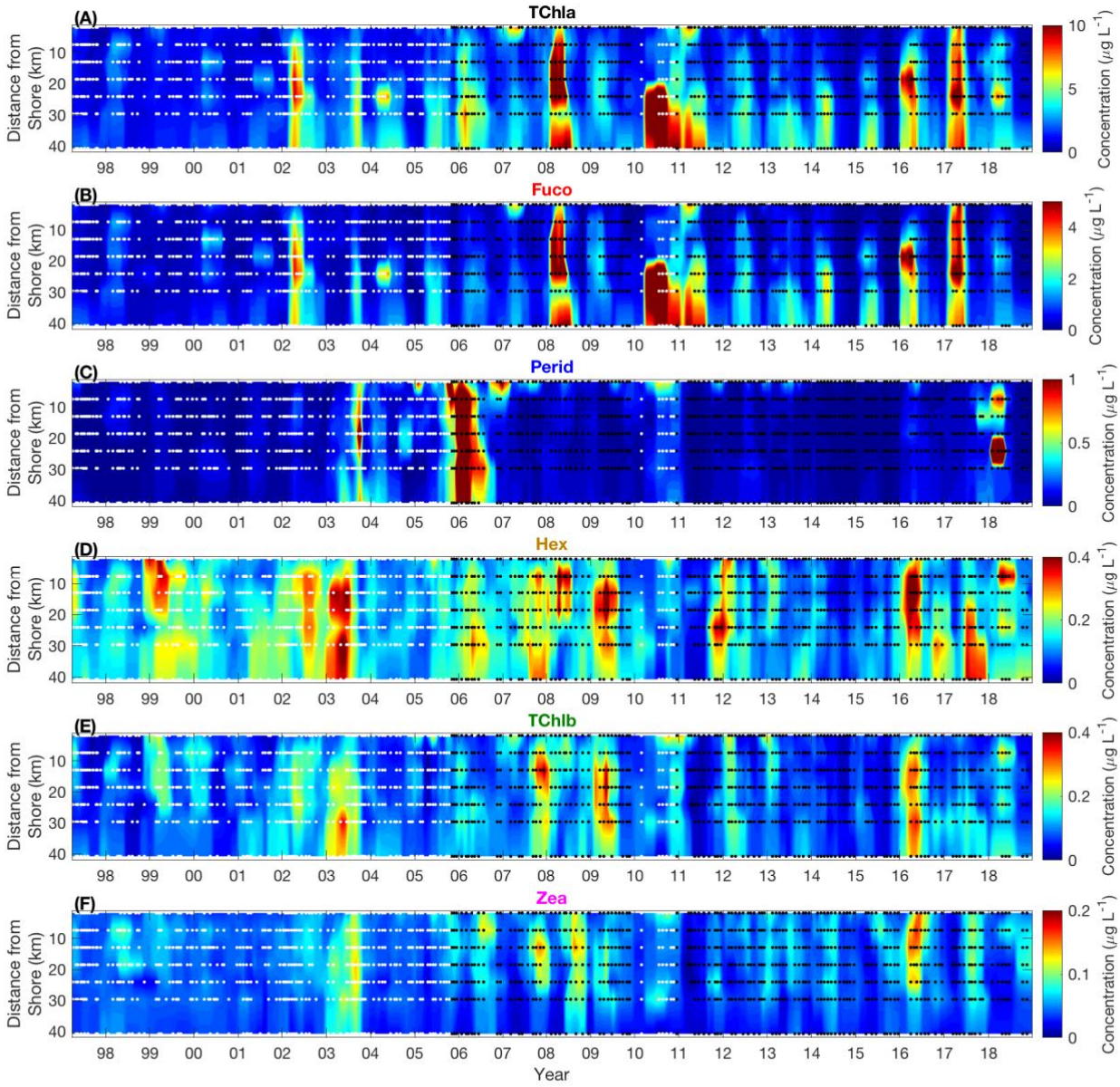

Figure 5. Spatiotemporal dynamics of (A) TChla, (B) Fuco, (C) Perid, (D) Hex, (E) TChlb, and (F) Zea. The top of each panel corresponds to PnB station 1 on the mainland shelf. White dots show modeled pigment concentrations, while black dots show pigment concentrations measured by HPLC. Ordinary kriging with an exponential-Bessel fitting model (GLOBEC Kriging Software Package v3.0) was used to smooth the data for this figure. Interpolation length scales are 30 days and 5 km in the cross-shelf direction. Panel titles are color-coded as in Figure 2.

551 concentrations to the prymnesiophyte and chlorophyte biomarker pigments, the dynamic range

552 and variance in Perid was high (Table 3). Dinoflagellate biomarker pigment concentrations

553 (Perid) showed the weakest correlations with other biomarker pigment concentrations (Table 3).
554 The prymnesiophyte and chlorophyte biomarker pigment concentrations, Hex and TChlb, were
555 strongly correlated with one another, though Hex was found at significantly higher
556 concentrations on average (Table 3; two-sample t-test, $p < 0.001$). The picophytoplankton
557 biomarker pigment Zea was correlated with TChlb and Hex (Table 3), and was found at
558 significantly lower concentrations (two-sample t-test, $p < 0.001$ in all comparisons) and
559 displayed the smallest dynamic range of the five biomarker pigments (Table 3).
560 Fuco showed a clear seasonal cycle with blooms in the spring and annual minima in the
561 fall (Figure 5B and 6B). The magnitude of spring diatom blooms increased later in the time
562 series, beginning in 2008. Spatial variations in diatom pigment concentrations were also
563 apparent, with higher concentrations often observed at the southern PnB stations relative to those
564 closer to the mainland coast. Large diatom bloom events were observed in the PnB record in
565 2002, 2008, 2010, 2016, and 2017, while relatively low Fuco concentrations were observed
566 consistently from 1997-2001. Conversely, dinoflagellate concentrations periodically increased at
567 PnB station 1, but were typically observed at low concentrations at all other stations (Figure 5C).
568 Anomalous SBC-wide dinoflagellate blooms were observed in late 2003 and early 2006, and
569 again in late 2017 and early 2018. Years with pronounced dinoflagellate blooms typically
570 coincided with an apparent suppression of diatom blooms.
571 Of the five PGs investigated, the biomarker pigments for prymnesiophytes and
572 chlorophytes, Hex and TChlb, showed the most similar dynamics to one another (Figure 5D and
573 5E, Table 3). These PGs were typically at their highest concentrations in the winter and early
574 spring, but also sporadically increased at other times of year. Picophytoplankton biomarker
575 pigment concentrations (Zea) generally followed the opposite pattern of that observed in Fuco,

with relatively high concentrations observed in the summer and fall and at the northern PnB stations (Figure 5F).

3.2. PG Seasonal Cycles

Mean seasonal cycles for each PG were calculated by computing monthly mean pigment concentrations after averaging by cruise (spatially) and then, where multiple cruises occurred in the same month, by month (Figure 6). The strongest seasonality (> 4-fold difference in annual maximum and minimum) was observed in Fuco, which exhibited annual maxima in April and May (monthly mean concentrations ~2 µg L^{-1}) and minima in the fall and winter (mean concentrations < 0.5 µg L^{-1}). On average, TChlb concentrations were relatively high from December to June (maximum of ~0.15 µg L^{-1} in March), and low from July to October (minimum of ~0.07 µg L^{-1} in September). Similarly, Hex concentrations were high in winter and spring (~0.2 µg L^{-1} maximum), and

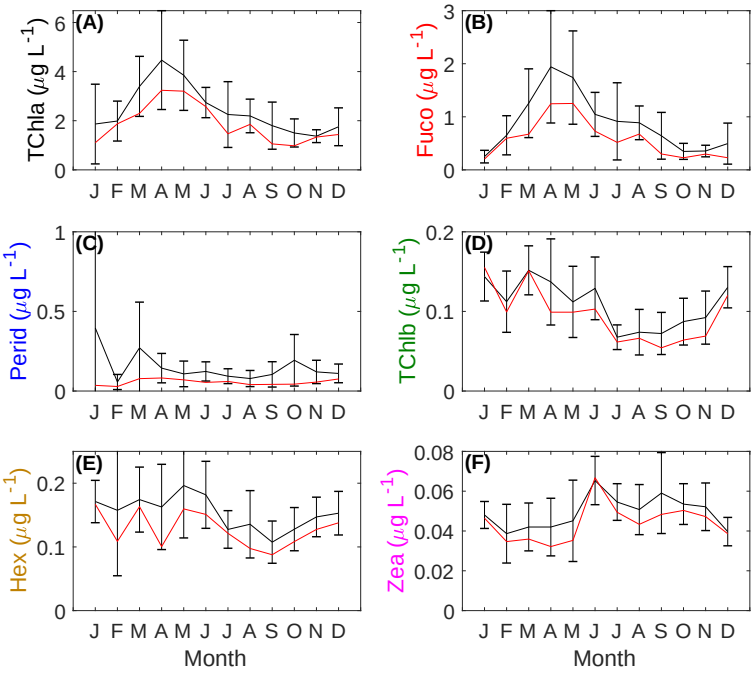

Figure 6. Mean +/- 95% confidence intervals (black) and median (red) annual cycles of (A) TChla, (B) Fuco, (C) Perid, (D) TChlb, (E) Hex, and (F) Zea. Annual cycles were computed based on each pigments monthly mean time series determined by averaging each pigments' concentrations by sampling event and when more than one sampling event occurred in the same month, by month. Y-axis labels are color-coded as in Figure 2.

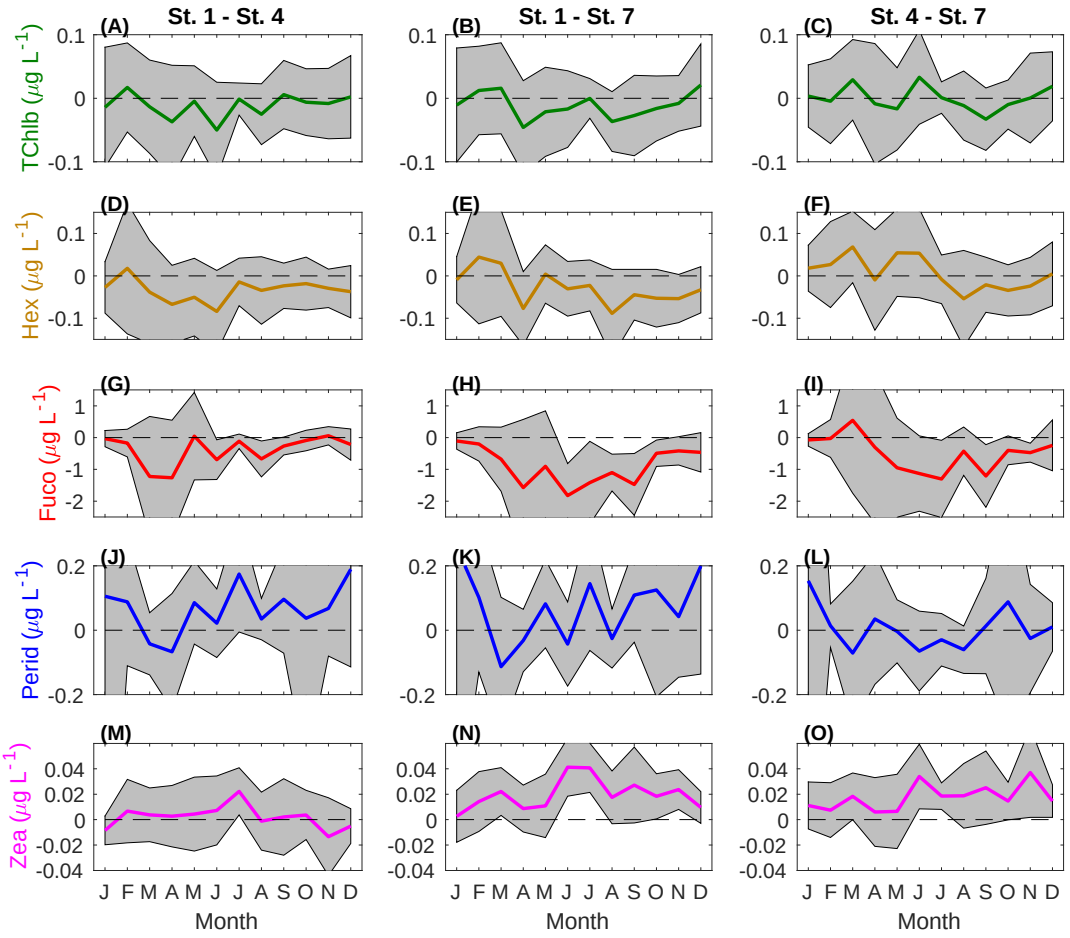

Figure 7. Spatial differences in mean annual cycles across PnB stations (A, D, G, J, M) 1 and 4, (B, E, H, K, N) 1 and 7, and (C, F, I, L, O) 4 and 7, for the five major biomarker pigment concentrations. The shaded region around each line corresponds to the 95% confidence interval computed for the difference of monthly mean pigment concentrations. Significant differences in monthly mean pigment concentrations at 95% confidence thus occur where the shaded region does not overlap the dashed zero line. Y-axis labels and lines are color-coded as in Figure 2.

599 lowest in September (~0.1 µg L^{-1}). Seasonality in Zea was less pronounced, though relatively

600 high concentrations were observed from June to October (annual maximum ~0.06 µg L^{-1}, annual

601 minimum ~0.04 µg L^{-1}). Finally, any potential seasonality in Perid concentrations was not

602 resolvable due to a combination of the predominantly decadal variations observed here (Figure

603 5C), the bio-optical model's poor performance in reconstructing smaller-scale Perid variations

604 (Figure 4; Table 2), and the coarse sampling resolution available in this data set (see Section 4.2
605 below for further discussion).

606 We investigated cross-SBC variability in each PGs annual cycle by quantifying monthly
607 climatologies for each pigment at each PnB station. Past observations of regional advection
608 patterns and satellite sea-surface temperature and chlorophyll *a* concentrations suggest that the
609 southern PnB stations (PnB station 7 is the southern-most) are generally associated with
610 relatively cool, recently upwelled waters, while the northern PnB stations (e.g., PnB station 1)
611 are associated with warmer surface waters and lower chlorophyll concentrations on average
612 (Harms and Winant, 1998; Henderikx Freitas et al., 2017). These cross-SBC differences are
613 driven by a combination of the upwelling shadow downwind of the coastal Santa Ynez
614 mountains, the physical concentration of phytoplankton by the persistent, convergent eddy in the
615 SBC, and differences in the relative advection of southern CCS and SCBight waters (Harms and
616 Winant, 1998; Simons et al., 2015; Henderikx Freitas et al., 2017). Figure 7 shows the mean +/-
617 95% confidence intervals in the difference of monthly mean pigment concentrations between
618 stations 1 and 4 (northern vs. central SBC), 1 and 7 (northern vs. southern SBC), and 4 and 7
619 (central vs. southern SBC).

620 Amongst the 5 PGs, the largest spatial variations in seasonality were observed for the
621 diatom biomarker pigment, Fuco (Figure 7). Fuco concentrations at station 7 were significantly
622 higher than those at station 1 from June through October, with monthly mean differences of
623 nearly 2 µg L^{-1} at times (Figure 7H). Fuco concentrations were also significantly higher (> 1 µg
624 L^{-1} in magnitude) at station 7 relative to station 4 in July, and on average were higher, though not
625 always significantly higher, from April through December (Figure 7I). The opposite pattern was
626 observed in the spatial variations in the annual Zea cycle (Figure 7M-O). Higher Zea

concentrations were observed at station 1 and 4 relative to station 7. These differences were most pronounced and often statistically significant from June to December, while differences in monthly mean Zea concentrations between stations 1 and 4 were generally small. Spatial variations in monthly mean concentrations of TChlb and Hex were relatively small and almost never statistically significant. However, the monthly mean concentrations of both of these pigments were typically lower at station 1 than at stations 4 and 7, except for during the winter and early spring (Figure 7A-F). Dinoflagellates exhibited the opposite pattern, with higher monthly mean Perid concentrations typically found at station 1 relative to stations 4 and 7. However, these differences were never statistically significant due likely to the large amount of variability in Perid on interannual time scales (Figure 7J-L).

3.3. Climate forcings and interannual to multi-decadal PG variations

Several notable shifts in the phases of the three major modes of North Pacific climate variability, the ENSO, NPGO, and PDO, occurred during the study period and were linked to interannual variability in some PGs (Figures 8 and 9). Due to their association with a suppression of upwelling winds and water column mixing, extreme El Niño events are expected to result in anomalously low concentrations of the upwelling-responsive PGs (Bograd and Lynn, 2001; Chavez et al., 2002; Venrick, 2012). Such events occurred in 1997-1998 and again in 2015-2016. Mild El Niño events, associated with less severe oceanographic impacts, were also observed in the late fall and early winter of 2002 to 2003, 2004 to 2005, 2006 to 2007, and 2009 to 2010 (Figure 8A-B). Conversely, notable La Niña events, which are expected to enhance upwelling

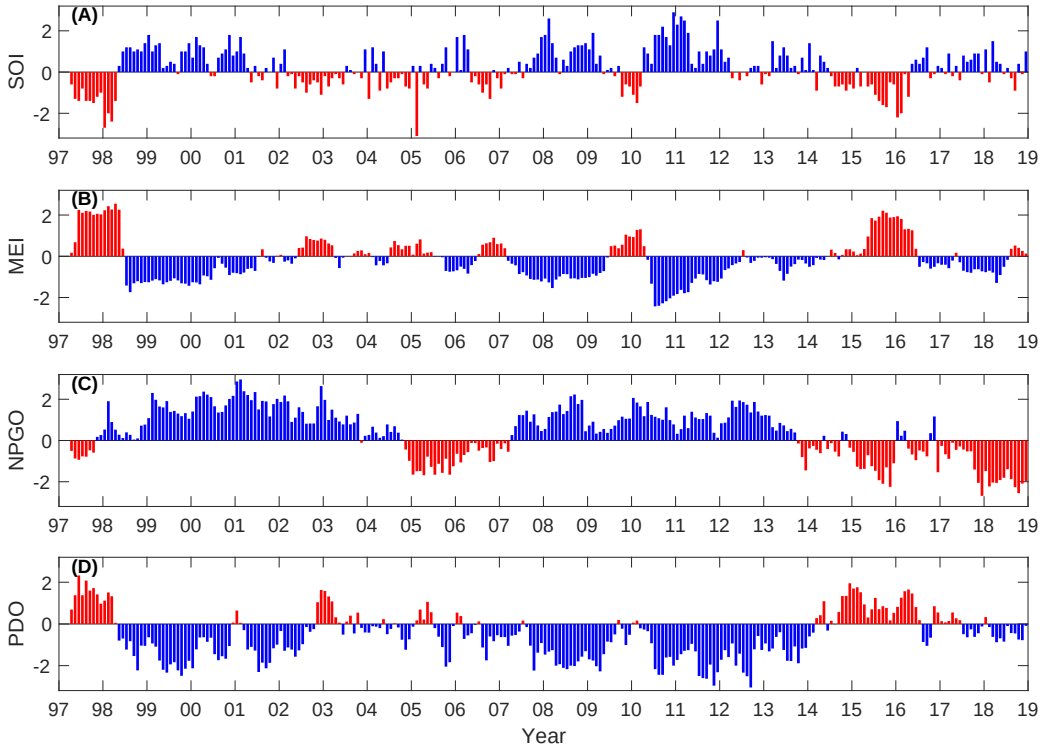

Figure 8. Indices of the dominant modes of North Pacific climate variability, including the (A, B) El Niño Southern Oscillation represented by the (A) Southern Oscillation Index (SOI) and the (B) Multivariate ENSO Index (MEI), (C) the North Pacific Gyre Oscillation (NPGO), and (D) the Pacific Decadal Oscillation (PDO). Blue and red bars indicate "cold" and "warm" phases, respectively.

and result in positive anomalies for most PGs, occurred from 1999 to early 2001, 2007 to 2009, and 2010 to 2011.

Relative to the ENSO, both the NPGO and PDO vary on longer time scales. The oceanographic impacts of the NPGO and PDO are less well studied than those of the ENSO, but generally, the PDO is thought to alter the timing and reduce the amplitude of seasonal upwelling and to drive a relaxation of the California Current in the northern CCS (Mantua and Hare, 2002; Di Lorenzo et al., 2013), while the NPGO has the same impact on the southern CCS and SCBight (Di Lorenzo et al., 2008; Di Lorenzo et al., 2013). The majority of the study period overlapped with the cold phases of both the NPGO and PDO (Figure 8C-D). However, the

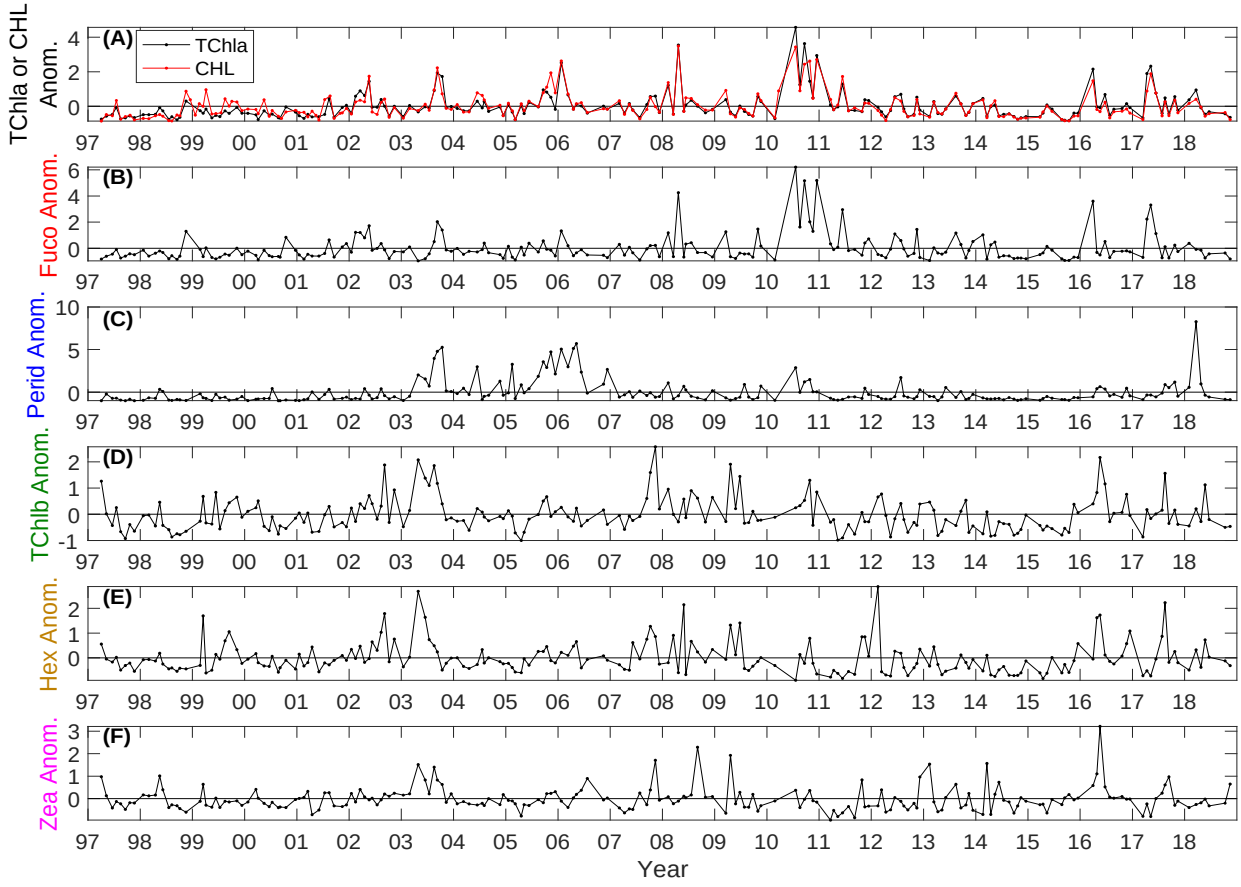

Figure 9. Normalized seasonal anomaly time series for (A) TChla (black) and fluorometric CHL (red), (B) Fuco, (C) Perid, (D) TChlb, (E) Hex, (F) Zea. Anomalies are computed by subtracting the climatological mean pigment concentrations shown in Figure 6 from each pigment concentration's monthly mean time series, and then normalizing to the climatological mean pigment concentration. Anomalies are thus unitless and represent a fold-change from the annual cycles shown in Figure 6. Y-axis labels are color-coded as in Figure 2.

NPGO briefly shifted to its warm phase from 2005 to early 2007, and again returned to a warm phase for the last five years of the record (Figure 8C). Over the course of the study period, the longest sustained warm phase of the PDO was observed from 2015 to 2017. The PDO was also briefly in its warm phase at the start of the record, and apart from a neutral phase from 2003 to 2006, remained in its cold phase throughout the remainder of the study period (Figure 8D).

Notably, both HPLC and bio-optically modeled pigment observations partially overlapped with

both cold and warm phases of all three climate oscillations considered here (Supp. Figure S1). While the model training data were biased toward some phases of these climate oscillations (particularly cold phase of the PDO), the model validation results (Figure 4, Supp. Figures S6 and S7) indicate that this bias does not impact model fidelity.

Interannual variations in the seasonal cycles of each PG and in TChla and CHL were investigated by computing anomalies in the concentrations of each biomarker pigment relative to its monthly climatology (Figure 9). After subtraction of each pigment's monthly climatology, anomalies were normalized to monthly mean pigment concentrations so that the anomalies shown in Figure 9 represent a unitless fold-change relative to the monthly climatologies shown in Figure 6.

In general, low anomalies in all five biomarker pigment concentrations were observed for the first five years of the time series (Figure 9). While this period of the time series considers pigment concentrations modeled using the Perkin-Elmer spectrophotometer (see Sections 2.4 and 2.6 above), anomalies in fluorometrically determined CHL concentrations mirror those in modeled TChla concentrations, suggesting these patterns are valid (Figure 9A). A notable commonality amongst the anomaly time series of all PGs except picophytoplankton was the persistence of negative anomalies from 1997-1998 and from 2014-2015. These observations coincided with the two largest El Niño events sampled during this time series (Figure 8), and the latter event was preceded by the extraordinary marine heat wave known as the "warm blob" (Bograd and Lynn, 2001; Bond et al., 2015; Jacox et al., 2016). However, some of the largest positive anomalies in the time series of all 5 biomarker pigments were observed in 2016 while the second extreme El Niño persisted (Figures 8 and 9). More generally, high correlations amongst the anomaly time series of the prymnesiophyte, chlorophyte, and picophytoplankton

686 biomarker pigments were found (Table 4). Conversely, the largest anomalies in diatom and
687 dinoflagellate biomarker concentrations generally did not co-occur. Further, the diatom and
688 dinoflagellate anomaly time series were only weakly correlated with one another and with the
689 other PGs (Table 4).

690 The largest positive diatom biomarker pigment anomalies were observed in 2008, 2010,
691 2011, 2016, and 2017 (Figure 9B). Relatively large La Niña events were observed in conjunction
692 with the cold phases of the NPGO and PDO in 2008, 2010, and 2011, which may partially
693 account for these anomalous events (Figure 8). However, a similar alignment of the ENSO,
694 PDO, and NPGO also occurred from 1999-2001 with no concurrent observations of anomalous
695 diatom blooms (Figures 8 and 9B), suggesting that a complex combination of local and climate
696 forcings are responsible for driving anomalous diatom blooms in the SBC. The highest
697 dinoflagellate anomalies were observed in 2003, 2006, and 2018 (Figure 9C). Taking into
698 account the lack of a resolvable annual cycle in dinoflagellates (Figure 6C), this indicates a
699 roughly decadal pattern in dinoflagellate biomarker pigment concentrations corroborated by
700 previous studies in the SCBight and CCS (Gregorio and Pieper, 2000; Smayda and Trainer,
701 2010; Fischer et al., 2020). Notably, positive dinoflagellate anomalies were observed during
702 most cruises from 2003 to late 2006, in 2010, and from late 2017 to early 2018; these time
703 periods mostly co-occurred with a negative NPGO index (Figure 8C). The largest positive
704 anomalies in prymnesiophyte pigment concentrations occurred in 2003 and 2012, while the
705 largest chlorophyte pigment anomalies were observed in 2002-2003, 2007, 2009, and 2016
706 (Figure 9D and 9E). Finally, the largest anomalies in picophytoplankton pigment concentrations
707 were observed from 2007-2009 and in 2016 (Figure 9F). The prymnesiophyte, chlorophyte, and
708 picophytoplankton biomarker pigment anomalies did not demonstrate noticeable event-scale

responses to climate forcings other than the previously described suppression of prymnesiophyte and chlorophyte biomarker pigment concentrations during El Niño events (Figures 8 and 9).

Table 4. Pearson's correlation coefficients amongst normalized pigment anomaly time series (see Figure 9). Insignificant correlations ($p > 0.05$) are not shown.

Pigment	TChlb	Hex	Fuco	Perid	Zea
TChla	0.29		0.94	0.43	
TChlb		0.71		0.17	0.65
Hex			-0.14	0.17	0.45
Fuco				0.19	
Perid					0.17

We assessed long-term trends in total chlorophyll *a* (Figure 9A) and biomarker pigment concentration anomaly time series (Figure 9B-F), and for monthly anomalies computed separately for each PnB station, using the modified Mann-Kendall trend test for autocorrelated time series outlined in Hamed and Rao (1998) (Supp. Table S2). With the exception of decreasing long-term trends in Hex at PnB stations 2, 3, and 6, no statistically significant ($p < 0.05$) trends were found for any of the pigments considered (Supp. Table S2). The spatial incoherence of the significant long-term trends in Hex makes them difficult to interpret and suggests they may be due to stochastic variability rather than any oceanographic or climate forcing considered here.

3.4. Associations of PGs with oceanographic forcings

We performed empirical orthogonal function (EOF) analysis to determine the dominant modes of association amongst the five biomarker pigments and other oceanographic parameters (Temp, Sal, NO_3, PO_4, and $Si(OH)_4$, representing temperature, salinity, nitrate, phosphate, and silicate, respectively; Figure 10). EOF analysis as applied here is synonymous with principal components analysis and decomposes the data set into a series of orthogonal modes. Each mode

730 is characterized by a set of loadings, or weights, describing the contribution of each variable to
731 the mode (Figure 10A-D), and an amplitude function describing the variability of that mode
732 through time (Figures 10E-H and 11) and, though not considered here, space (Thomson and
733 Emery, 2014). Each mode explains a known fraction of the variance in the original data set, with
734 the first mode accounting for the largest proportion of the total variance and higher order modes
735 accounting for sequentially less variance. For the EOF analysis shown here, all variables were
736 averaged by cruise (spatially) and, where multiple cruises occurred in the same month, by month,
737 to create a monthly time series of each variable as above. Monthly time series of each variable

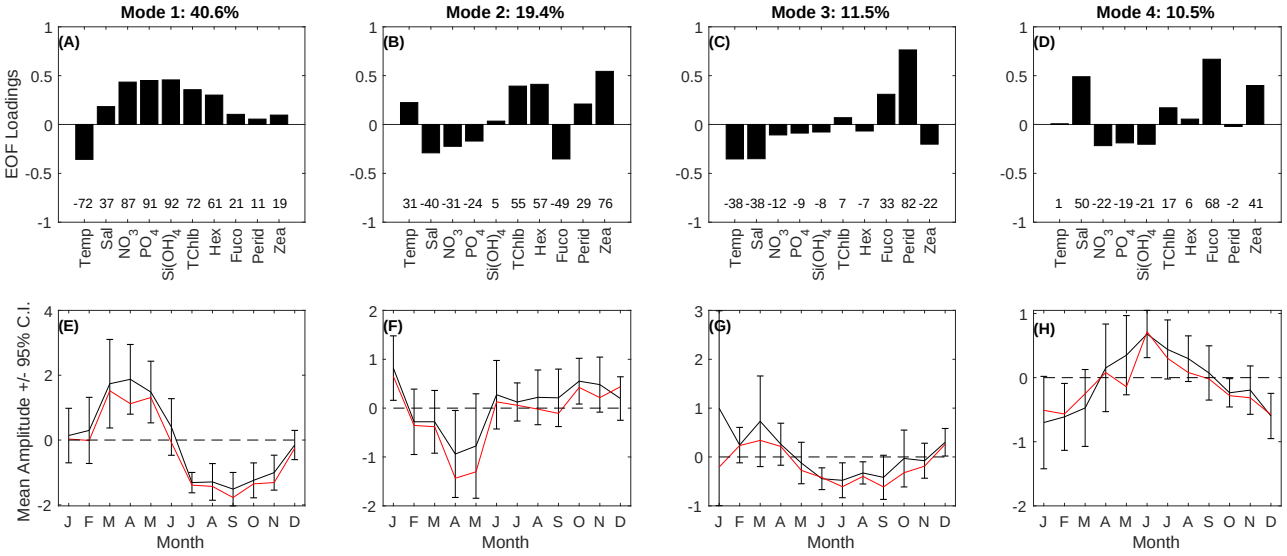

Figure 10. (A, B, C, D) Loadings and (E, F, G, H) mean +/- 95% confidence intervals (black) and median (red) annual cycles of the amplitude functions of the first four EOF modes of the pigment-oceanographic data set. The variance explained by each mode is indicated in the title of each panel. Numbers above each x-tick are the correlation coefficient between a particular EOF mode amplitude function and variable multiplied by 100. All variables were averaged by sampling event (spatially) and, where multiple cruises occurred in the same month, by month, to create a monthly time series of each variable. Monthly time series were then z-scored prior to computing EOFs.

738 were then standardized to zero mean and unit variance prior to computing EOFs. The first four
739 EOF modes cumulatively explained 82% of the variance in the data set, partitioned across modes
740 1, 2, 3, and 4 as follows: 40.6%, 19.4%, 11.5%, 10.5%. Modes 5 and 6 explained 6.5 and 5.3%

741 of the variance in the data set, respectively, and all higher order modes explained < 3% of the
742 variance. Modes 5 and 6 are thus not considered here.

743 The results of the EOF analysis demonstrate the importance of seasonal upwelling
744 responses in driving the variations of the five PGs. The loadings of EOF Mode 1 were positive in
745 the 3 macronutrient concentrations, salinity, TChlb, and Hex, negative in temperature, and only
746 weakly positive for diatom, dinoflagellate, and picophytoplankton pigment concentrations
747 (Figure 10A). This demonstrates a relatively strong covariance amongst chlorophyte and
748 prymnesiophyte pigment concentrations and cold, saline, nutrient-rich waters, indicating rapid
749 positive responses of these PGs to recent upwelling. The mean seasonal cycle of EOF Mode 1
750 amplitudes confirmed that this mode represents an early upwelling oceanographic state, with the
751 highest monthly mean values observed from March through May and annual minima observed in
752 the late summer and early fall (Figure 10E).

753 The loadings of EOF Mode 2 were positive in temperature and in all PG biomarker
754 pigment concentrations except for diatoms, and negative in diatom pigment concentrations,
755 salinity, nitrate and phosphate (Figure 10B). This loading pattern indicates contrasting ecosystem
756 states with negative amplitudes corresponding to an upwelling-driven diatom bloom, and
757 positive amplitudes indicating a stratified water column favoring a mixed assemblage dominated
758 by pico- and nano-phytoplankton. Inspection of the mean seasonal cycle of Mode 2 amplitudes
759 again confirmed this interpretation, with annual minima (indicating a diatom bloom) observed in
760 April and May and maxima observed in October and November (Figure 10F). Taken together,
761 EOF Modes 1 and 2 demonstrate that ~60% of the variance in the combined PG and
762 oceanographic data set is explained by the progressive response of the environment and
763 phytoplankton community to upwelling.

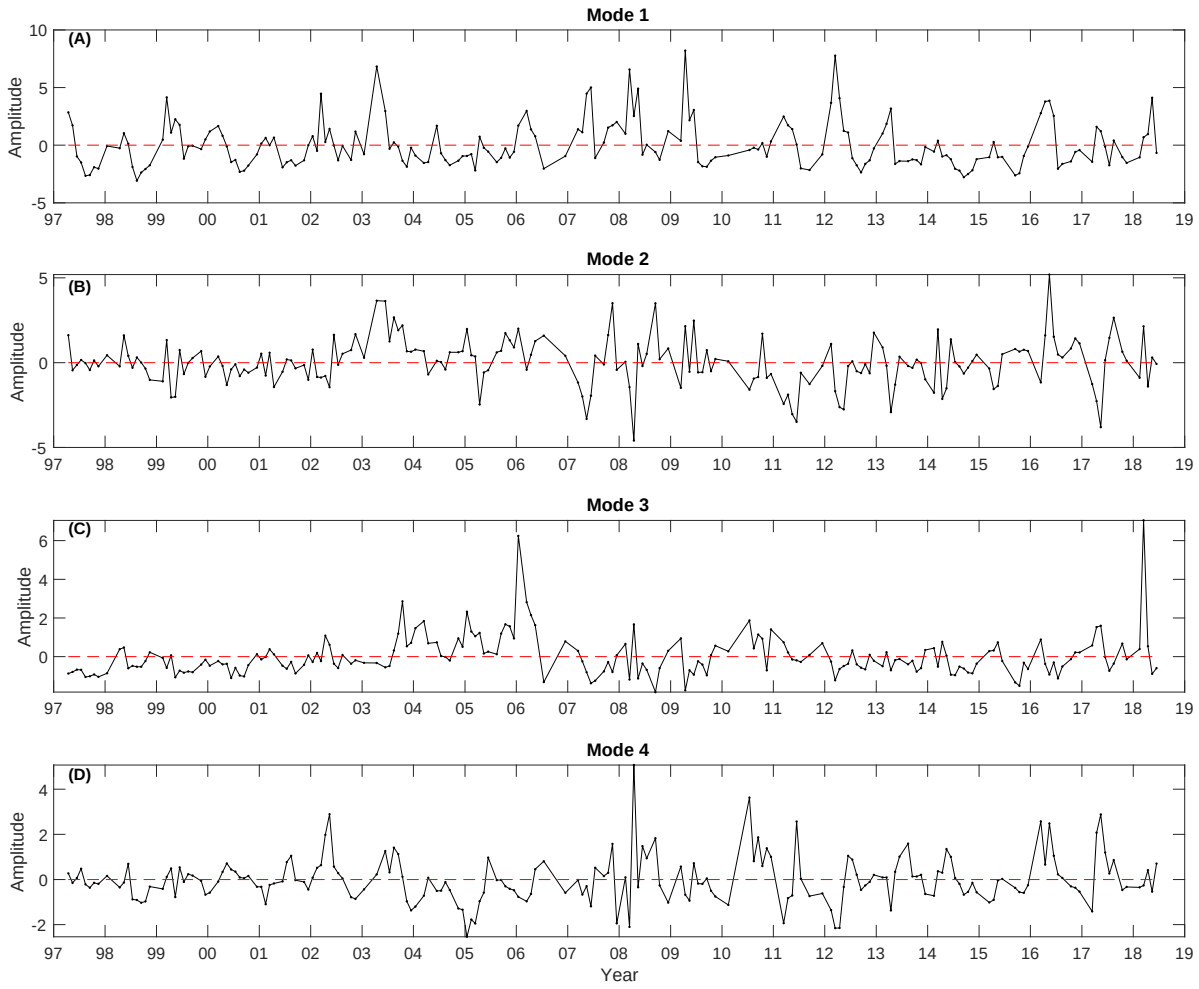

Figure 11. Amplitude time series of the first four pigment-oceanographic EOF modes.

764 EOF Mode 3 also exhibited some seasonality, but did not appear strongly linked to
765 upwelling dynamics. The loadings of EOF Mode 3 were strongly positive for Perid and to a
766 lesser extent Fuco, while negative loadings were found for both temperature and salinity (Figure
767 10C). The loadings for the other variables were small indicating relatively weak associations of
768 this mode with the other PGs, as well as with macronutrient concentrations. The mean seasonal
769 cycle of EOF Mode 3 showed positive monthly mean amplitudes during the winter and early
770 spring and negative amplitudes from spring through fall (Figure 10G). This observation in
771 conjunction with the covariance of temperature and salinity loadings in opposition to

772 dinoflagellate pigment concentrations suggests that this mode is associated with winter-time
773 precipitation and freshwater discharge events. Such events are thought to provide favorable
774 conditions for inner-shelf dinoflagellate blooms across the broader California coast (Gregorio
775 and Pieper, 2000; Fischer et al., 2020).

776 EOF Mode 4 showed positive loadings for diatom and picophytoplankton biomarker
777 pigment concentrations and salinity, in opposition to weak negative loadings in the three
778 macronutrient concentrations (Figure 10D). The mean annual cycle in EOF Mode 4 amplitudes
779 was positive from May to August with an annual maximum in June, and negative throughout late
780 fall, winter, and early spring (Figure 10H). Interpretation of this mode is complicated by the
781 unexpected covariance of diatom and picophytoplankton pigment concentrations with high
782 salinities, but not the other oceanographic properties, and the potential for the orthogonality
783 constraint of EOF analysis to obscure true oceanographic signals with noise in higher order
784 modes. However, the combination of the observed loading pattern and mean seasonal cycle
785 suggests that this mode may represent a transitional state from a senescing spring diatom bloom
786 to a stratified, picophytoplankton-dominated system. Such a transitional state may be driven by
787 unusually late seasonal upwelling, enhanced entrainment by the persistent cyclonic eddy in the
788 SBC, or some combination of these and other forcings. Inspection of the amplitude time series
789 shows that the highest positive amplitudes of this mode often do not co-occur with the largest
790 negative amplitudes of EOF Mode 2 (which indicates a well-developed diatom bloom), but do
791 co-occur with some of the most anomalous Fuco concentrations observed on PnB (Figures 9B
792 and 11D). Examples of this pattern are most prominent in 2002, 2010, and 2016. Taken together,
793 these results suggest this mode represents a unique diatom bloom state associated with
794 potentially different forcings than the diatom bloom state depicted in EOF Mode 2.

795

796 **3.5. Impacts of climate forcings on PGs and oceanographic modes**

797 Previous work has demonstrated significant impacts of the El Niño Southern Oscillation
798 (ENSO) and the two major modes of Pacific decadal climate variability, the Pacific Decadal
799 Oscillation (PDO) and the North Pacific Gyre Oscillation (NPGO), on coastal California
800 oceanography and marine ecosystems (Mantua et al., 1997; Bograd and Lynn, 2001; Chavez et
801 al., 2002; Di Lorenzo et al., 2008; Venrick, 2012; Di Lorenzo et al., 2013; Jacox et al., 2016;
802 Fischer et al., 2020). Less is known about the impacts of these climate oscillations on PG
803 dynamics in the SBC (Anderson et al., 2008; Venrick, 2012; Barth et al., 2020; Fischer et al.,
804 2020), though the qualitative associations with the PG biomarker pigment concentrations
805 described above indicate non-negligible impacts (Figures 8 and 9). To further investigate the
806 roles of these climate oscillations in driving event-scale PG variations in the SBC, conditional
807 averages of the seasonal anomalies of each biomarker pigment and EOF mode amplitude
808 function (Figure 12) were computed for the 15% largest positive and negative values of each of
809 the four climate indices (the Southern Oscillation Index, or SOI, and Multivariate ENSO Index,
810 or MEI, provide two independent indices of ENSO) overlapping with the biomarker pigment
811 (Figure 12A-E) and pigment-oceanographic time series used to compute EOFs (Figure 12F-I).
812 Statistically significant differences between conditionally averaged pigment concentrations or
813 EOF mode amplitudes were assessed using two-sample t-tests.

814 The impacts of ENSO events on the dynamics of specific PGs and PG-oceanographic
815 EOF modes were evident in the conditional averaging of PG biomarker pigment and EOF mode
816 amplitude anomalies (Figure 12). As expected, diatom pigment concentrations showed positive
817 anomalies during La Niña events and negative anomalies coincident with El Niño events. These

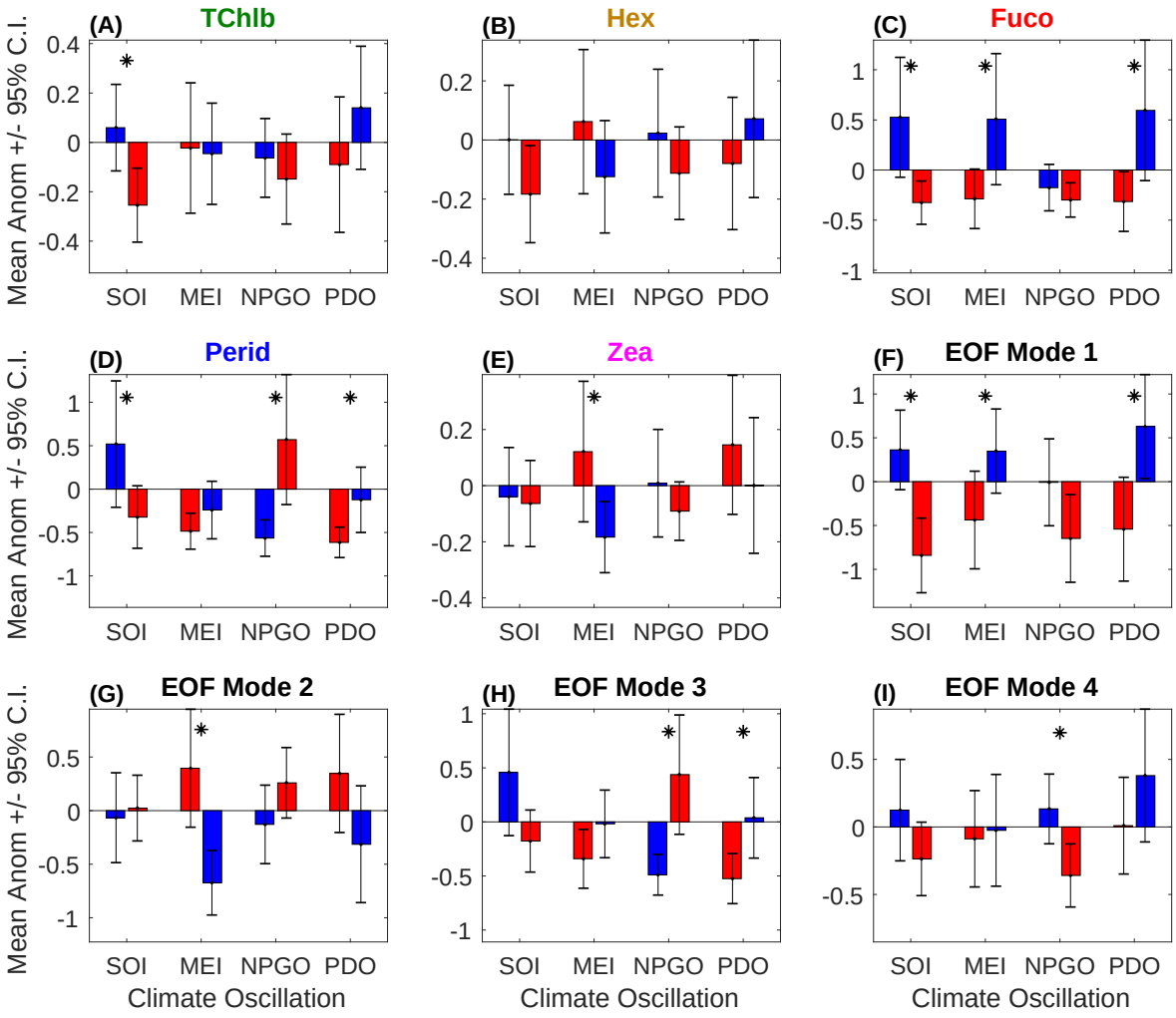

Figure 12. Conditional mean +/- 95% confidence intervals of biomarker pigment concentration and EOF amplitude anomalies according to the 15% largest positive and negative values of the Southern Oscillation Index (SOI), Multivariate ENSO Index (MEI), North Pacific Gyre Oscillation index (NPGO), and the Pacific Decadal Oscillation index (PDO). Red and blue bars indicate the "warm" and "cold" phases of each climate oscillation. Pigment concentration anomalies are normalized to climatological mean values, while EOF mode amplitude anomalies are not as all variables were standardized prior to the EOF analysis. Stars above each bar group indicate statistically significant ($p < 0.05$) differences across the warm and cold phase of the climate oscillation index according to a two-sample t-test. Panel titles are color-coded as in Figure 2.

818 impacts were consistent in both pattern and magnitude for both the SOI and MEI (Figure 12C),

819 and corroborated by significant correlations between Fuco and both the SOI and MEI (Table 5).

820 The impacts of the ENSO on the other biomarker pigments was less clear. Conditionally

averaged prymnesiophyte pigment concentration anomalies showed contrasting patterns across the two ENSO indices and neither difference was statistically significant, indicating no observable impact (Figure 12B). The patterns of conditionally averaged dinoflagellate pigment concentration anomalies across the SOI and MEI were similar, with La Niña events favoring higher concentrations, though the differences were not statistically significant (Figure 12D). Significantly higher (lower) anomalies were observed during La Niña events for the chlorophyte (picophytoplankton) biomarker pigment concentrations when considering the SOI (MEI), but no observable effects on these biomarker pigments were found according to the MEI (SOI) (Figure 12A and 12E). No significant correlations were found between TChlb or Zea with either the MEI or SOI (Table 5).

Table 5. Correlation coefficients of pigment concentration and pigment-oceanographic EOF mode amplitude anomalies with climate forcings. Pigment concentration anomalies are normalized to climatological mean values as in Figures 9 and 12. Insignificant correlation coefficients ($p < 0.05$) are not shown.

	SOI	MEI	NPGO	PDO
TChla	0.31	-0.27		-0.19
TChlb				
Hex				
Fuco	0.30	-0.26		-0.20
Perid			-0.22	
Zea				
Mode 1	0.20	-0.23	0.24	-0.25
Mode 2		0.19	-0.16	0.19
Mode 3	0.19		-0.26	
Mode 4			0.16	

The decadal modes of North Pacific Climate variability, the PDO and NPGO, also had variable impacts on the interannual dynamics of each PG. Significant differences were observed in conditionally averaged dinoflagellate pigment concentration anomalies for both the NPGO and PDO (Figure 12D). The magnitude of differences was greater for the NPGO and Perid was significantly correlated with the NPGO (Table 5) but was not significantly correlated with the

PDO, SOI, or MEI. Interestingly, high dinoflagellate anomalies were favored by the warm phase of the NPGO, but suppressed by the warm phase of the PDO. Conversely, the cold phase of the PDO significantly favored anomalously high diatom pigment concentrations, while the NPGO did not have an obvious impact on interannual Fuco variations (Figure 12C, Table 5). We observed no significant differences in conditionally averaged prymnesiophyte, chlorophyte, or picophytoplankton pigment concentration anomalies, and no significant correlations between these pigment concentration anomalies and the NPGO or PDO (Figure 12A, 12B, 12E, Table 5). However, higher anomalies in prymnesiophyte and chlorophyte pigment concentrations were observed during the cold phase of the PDO and NPGO relative to their respective warm phases.

Conditional averaging of the four EOF mode amplitude anomalies according to the 15% largest positive and negative values of the four climate oscillations that overlapped with the relevant pigment and oceanographic observations largely corroborated the results of the conditional averaging of the anomalies of each biomarker pigment (Figure 12F-I). EOF Mode 1, corresponding to an early-upwelling state with cold temperatures and high TChlb, Hex, and macronutrient concentrations, was significantly impacted by all three climate oscillations (Figure 12F, Table 5). The cold phase of all 3 climate oscillations favored anomalously strong upwelling and high chlorophyte and prymnesiophyte pigment concentrations. Similarly, the cold phases of the PDO, NPGO, and ENSO all favored negative amplitudes of EOF Mode 2, a proxy for diatom blooms, although the conditional averages were only significantly different for the MEI (Figure 12G). Correlations between EOF Mode 2 anomalies and the MEI, NPGO, and PDO were also significant (Table 5). Conditionally averaged values of EOF Mode 3 amplitude anomalies, interpreted as a dinoflagellate bloom mode associated with winter-time discharge events, showed significant impacts of both the NPGO and PDO, with the warm (cold) phase of the NPGO (PDO)

favoring anomalous dinoflagellate blooms (Figure 12H). Both indices of the ENSO suggested an enhancement of dinoflagellate blooms during La Niña events. These results were corroborated in part by significant correlations between EOF Mode 3 anomalies and the SOI and NPGO (Table 5). Finally, the transition state from a well-developed diatom bloom to a picophytoplankton dominated assemblage associated with high salinity surface waters, indicated by positive amplitudes of EOF Mode 4, was favored by cold phases of the ENSO, PDO, and NPGO, although significant differences in the conditionally averaged amplitudes of Mode 4, along with a significant correlation coefficient, were only observed for the NPGO (Figure 12I, Table 5).

4. Discussion

4.1. Summary of Results

We quantified seasonal to multi-decadal PG dynamics in the SBC based on an approximately monthly time series of HPLC and bio-optically modeled biomarker pigment concentrations spanning more than 20 years. The dominant SBC PGs resolvable from these HPLC pigment concentration data were identified using hierarchical cluster analysis and included diatoms, dinoflagellates, chlorophytes, prymnesiophytes, and picophytoplankton (Figure 2). The concentrations of five biomarker pigments, each assumed to represent the pigment biomass of one of the above PGs, were modeled with high fidelity using a previously developed bio-optical modeling approach (Table 2, Figures 3 and 4, Supp. Figures S6 and S7). Seasonal variations were resolvable for all PG biomarker pigments except Perid (representing dinoflagellates). On average, seasonal variations ranged from ~1.5-fold for the picophytoplankton, to ~2-fold for the prymnesiophytes and chlorophytes, to >4-fold for diatoms (Figure 6). The magnitude and patterns of each PG's annual cycle showed significant cross-SBC

887 differences (Figure 7). Relative to monthly mean biomarker pigment concentrations, interannual
888 variations were as high as 2-3-fold for picophytoplankton, prymnesiophytes, and chlorophytes,
889 and occasionally larger than 5-fold for both the diatoms and dinoflagellates (Figure 9). To the
890 extent that PG dynamics were associated with oceanographic forcings, upwelling exerted the
891 strongest control on PG dynamics (Figures 10 and 11). Natural climate oscillations including the
892 ENSO, PDO, and NPGO exhibited unique associations with each PG at the event scale (Figures
893 8, 9, 11, 12).

894 In the following, we discuss the limitations of the present study for assessing long-term
895 PG dynamics. We then explore the role of regional surface advection patterns in driving some of
896 our observations of seasonal to multi-decadal PG dynamics. Finally, we place our observations
897 of the associations of the dominant SBC PGs with oceanographic and climate forcings in the
898 context of broader knowledge of large-scale PG dynamics in the California Current System
899 (CCS), Southern California Bight (SCBight), and more generally in upwelling systems.

900

901 **4.2. Limitations of the present study – what are we missing?**

902 The assessments of seasonal to multi-decadal PG dynamics presented above rely on a
903 synthesis of HPLC and bio-optically modeled phytoplankton pigment concentrations to create a
904 22-year, approximately monthly record of PG biomarker pigment concentrations. We have
905 shown in Section 2.6 that the methods used to synthesize these two data sets are robust and well-
906 validated with independent data. However, several major limitations remain to be addressed in
907 order to use these data to assess seasonal to multi-decadal PG dynamics. Here, we discuss these
908 limitations and how they may impact our interpretations of the results presented above.

Like all methods for assessing PG dynamics, HPLC pigment analysis has strengths and weaknesses (Lombard et al., 2019). The prominent strengths of the HPLC method are demonstrated in our analysis: rigorously evaluated and standardized analytical procedures (Van Heukelem and Thomas, 2001; Hooker et al., 2010) enable precise and accurate PG observations with high spatiotemporal coverage; unique absorption signatures of biomarker pigments found in *in situ* and remotely sensed bio-optical properties allow biomarker pigment concentrations to be modeled with high skill, expanding the spatiotemporal coverage of observations (Chase et al., 2017; Catlett and Siegel, 2018); and the PGs resolved by pigment methods span a more holistic range of phytoplankton size classes than possible for many other methods.

However, HPLC (and bio-optically modeled) pigment concentrations also have widely-documented limitations and uncertainties (Higgins et al., 2011; Jeffrey et al., 2011). First, investigators must assume that biomarker pigment concentrations reasonably approximate the biomass of PGs. This assumption is applied explicitly here, and implicitly (often with additional assumptions) in studies employing more complicated pigment chemotaxonomy methods (Mackey et al., 1996; Uitz et al., 2006; Hirata et al., 2011). However, variability in pigment concentrations can arise due to a combination of changes in PG biomass, physiological responses to environmental conditions, and genetic or other sources of intra-PG variability (Higgins et al., 2011; Kramer and Siegel, 2019). In particular, the 1.5- to 2-fold seasonal variations observed in TChlb, Hex, and Zea above (Figure 6) fall within a range that could be explained by physiological variability in pigmentation (see Higgins et al., 2011, and references therein). Further, comparisons of PG dynamics inferred from photoprotective (Zea in the present analysis) and photosynthetic (including TChlb, Hex, Fuco, and Perid) pigments may be susceptible to biased interpretations given that these pigments vary differently in response to changing

irradiance (Higgins et al., 2011). However, the cluster analysis (Figure 2) shows that to first order, Zea covaries more strongly with DVChla (a photosynthetic pigment) than other photoprotective pigments, while photosynthetic biomarker pigments representative of other PGs covary with distinct suites of photoprotective pigments. These results suggest that variability in PG biomass is the first order determinant of the variations in biomarker pigment concentrations observed here.

Another limitation of biomarker pigment assessments is the ambiguity in the representation of a single PG by a particular biomarker pigment (Jeffrey et al., 2011; Kramer and Siegel, 2019). For example, the diatom biomarker pigment Fuco is also found in many other PGs, including the oft-abundant dinoflagellates, prymnesiophytes, and pelagophytes (Jeffrey et al., 2011). Bloom-forming dinoflagellates occasionally obscure the Fuco-diatom relationship in the SBC (Catlett et al., 2020b). This may partially explain certain anomalous Fuco observations in the present analysis, such as the ~2-fold anomaly in the fall of 2003 (Figure 9) and the covariation of Fuco with the dinoflagellate biomarker pigment Perid in EOF Mode 3 (Figure 10). Conversely, Perid is not found in some lineages of photosynthetic dinoflagellates and so is not representative of this entire PG (Jeffrey et al., 2011), which may partially explain the lack of a resolvable annual cycle in our results above (Figure 6). Finally, the underlying genetic, taxonomic, and functional diversity represented by each PG and biomarker pigment is highly variable. For example, the prymnesiophytes include a diverse array of functional groups including calcifiers like *Emiliania huxleyi*, DMS producers like *Phaeocystis sp.*, and mixotrophs like *Prymnesium parvum* (Nygaard and Tobiesen, 1993; Van Boekel and Stefels, 1993; de Vargas et al., 2007). Given their diverse functional roles and ecological niches, each of these prymnesiophyte species may be expected to respond differently to oceanographic and climate

forcings. Thus, the lack of clear associations of some PGs with oceanographic and climate forcings above may be explained in part by intra-PG variability in responses to these forcings.

The other primary limitation of the present study is that the monthly, unevenly sampled time series presented here does not capture short-term PG dynamics and failed to resolve some anomalous events. One known example of this is the unprecedented *E. huxleyi* bloom that occurred in the SBC in the first week of June, 2015 (Matson et al., 2019). After initial detection of the bloom in satellite imagery on May 31, 2015 (17 days after the PnB cruise in May, 2015), Matson et al. (2019) observed *E. huxleyi* cell concentrations on June 4, 2015 that were an order of magnitude greater than had ever been previously observed in the SCBight. Satellite imagery showed the bloom began decaying shortly after June 4 and had largely dissipated by the time PnB observed Hex concentrations similar to climatological mean values on June 18, 2015 (Matson et al., 2019; Figures 5D and 9E). There were likely additional anomalous blooms of specific PGs that were not sampled by PnB over the course of the 20+ year record presented here. The chronic under-sampling of January and February in this time series due to ship availability also leads to greater uncertainty surrounding typical winter-time PG concentrations in the SBC. Nonetheless, the broad seasonal and interannual patterns highlighted in the above analyses are likely robust to the imperfect sampling of the PnB time series and largely corroborate and complement existing observations of large-scale PG dynamics in the CCS and SCBight (see Section 4.4 below).

Finally, the 22-year biomarker pigment time series provides a rare glimpse into the climate forcings of interannual to multi-decadal PG dynamics. However, assessing the roles of the ENSO, PDO, and NPGO in driving interannual to decadal PG dynamics in the SBC remains difficult given the paucity of climate phase transitions and extreme events observed over the 22-

year biomarker pigment record. Only two strong El Niño events were sampled over the course of the time series, both of which coincided with warm phases of the NPGO and PDO (Figure 8). Similarly, both the NPGO and PDO remained in the cold phase for the majority of the 22-year time series, with only two significant, though relatively brief warm events sampled for each climate index. Further, the two warm PDO events coincided with extreme El Niño events, and the latter also coincided with the anomalous "warm blob" event in 2014-15 (Bond et al., 2015). Given these small sample sizes (despite the inclusion of 1393 stations sampled on 238 PnB cruises conducted over 22 years) and the potential for interactions amongst these climate oscillations, robust assessments of the impacts of the ENSO, PDO, and NPGO, as well as their interactions with one another and with anthropogenic climate forcing, on PG dynamics will require substantially longer time series than the 22-year record presented here. Nonetheless, the analyses above (Figures 8, 9, 12) provide an important step towards determining the roles North Pacific climate variability and anthropogenic climate forcing will play in determining SBC PG dynamics in the future.

4.3. Potential roles of advection in driving PG dynamics

The SBC's location in the transition zone between the upwelling-impacted, nutrient-rich waters of the CCS and the warmer, more oligotrophic waters of the SCBight, and the prevailing circulation patterns in and around the SBC (Harms and Winant, 1998; Winant et al., 2003; Dong et al., 2009; Brzezinski and Washburn, 2011), suggest that advection of source waters from these adjacent environments may impact observations of SBC PG dynamics. In general, upwelling winds intensify equatorward flows in the CCS and result in the advection of southern CCS waters into the western entrance of the SBC (Harms and Winant, 1998; Brzezinski and

1001 Washburn, 2011). The relaxation of upwelling winds allows for a return flow of SCBight waters
1002 poleward along the mainland coast and into the eastern entrance of the SBC (Harms and Winant,
1003 1998; Melton et al., 2009). On longer time scales, the NPGO appears related to variations in the
1004 balance of these two flows in the southern CCS and SCBight (Di Lorenzo et al., 2008; Di
1005 Lorenzo et al., 2013).

1006 While there is high variability in surface ocean circulation patterns in and around the
1007 SBC, direct observations of surface currents and spatial patterns of satellite sea surface
1008 temperature and chlorophyll *a* concentrations apparently confirm that the southern and western
1009 portions of the SBC tend to be more heavily impacted by CCS waters, while the northern and
1010 eastern SBC are more frequently impacted by SCBight waters (Harms and Winant, 1998;
1011 Henderikx Freitas et al., 2017). In conjunction with past studies showing more frequent
1012 dominance by diatoms (dinoflagellates) in CCS (SCBight) waters (Venrick, 2002; Venrick,
1013 2012; Taylor et al., 2015), our observations of the prominent spatial variations in PG seasonality
1014 (Figure 7), as well as the decadal dinoflagellate anomalies associated with the NPGO (Figures 8,
1015 9, 11, and 12), suggest an important role of advection in driving seasonal to multi-decadal PG
1016 dynamics in the SBC.

1017 Here we employ a Lagrangian particle tracking model within a high resolution ROMS
1018 solution for a 10-year subset (2004-2013) of the PG time series to investigate whether variations
1019 in source water origin alters phytoplankton community composition in the SBC (see Section
1020 2.8.2). Particles were tracked backwards in time from 34 release points along the PnB transect on
1021 each day of the 10-year time series. Figure 13 shows examples of particle trajectories projected
1022 backwards in time for two different days of the time series where a majority of particles
1023 originated from the West origin box (Figure 13A) or the East origin box (Figure 13B). These

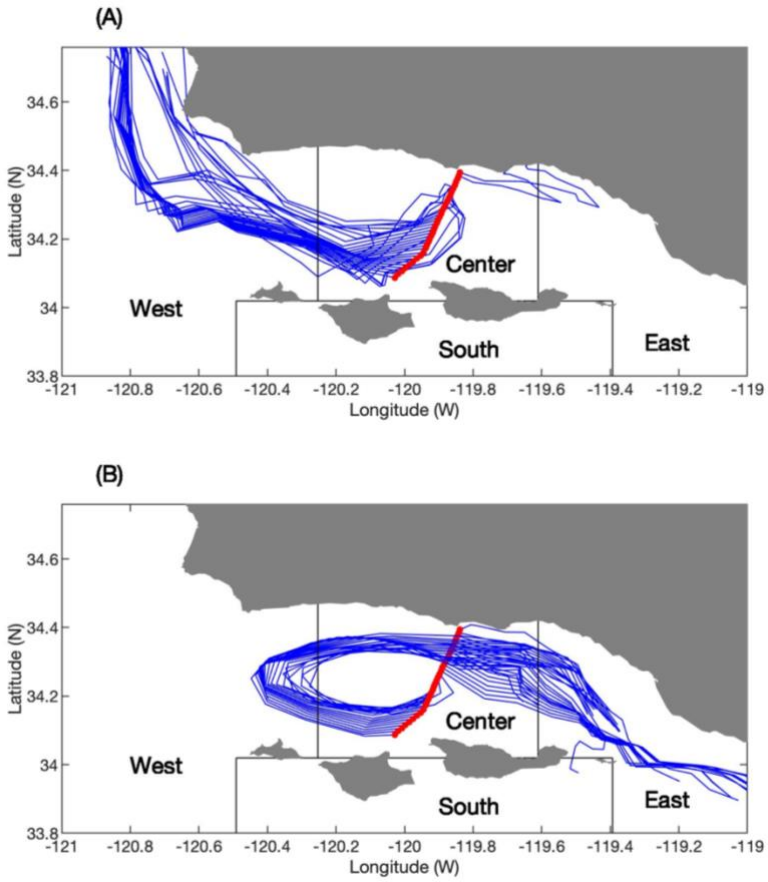

Figure 13. Example 10-day reverse-tracking particle trajectories simulated by the ROMS particle tracking model on (A) April 3, and (B) April 23, 2005. (A) shows typical particle trajectories during an upwelling event, with most particles originating from the West origin box, while (B) shows an upwelling-wind relaxation event driving higher advection of particles from the East origin box.

examples provide a synoptic view of advection patterns over a short-term (~2 week) upwelling-relaxation cycle, and support the assumption that on 10-day advection time scales, the proportion of particles advected from the West (East) origin box provides a reasonable approximation for the relative influence of southern CCS (SCBight) source waters on SBC PG dynamics. In order to align further analyses of the simulated particle trajectories with the approximately monthly sampling of PnB, monthly time series of the proportion of particles derived from each origin box for the PnB transect and for each PnB station were computed from the daily time series and are discussed here (see Section 2.8.2). All results considered here are for 10-day advection times; results from 5- and 15-day advection times are presented in Supporting Figures S9 and S10, and qualitatively agree with those shown here.

First, we used the simulated source water assessments to test the hypothesis that on seasonal time scales, cross-SBC variability in climatological mean diatom, dinoflagellate, and picophytoplankton pigment concentrations (Figure 7) are driven by variations in source water origin. Increased advection of CCS (SCBight) source waters is expected to lead to seasonally elevated diatom (dinoflagellate and picophytoplankton) concentrations. Figure 14A shows the mean annual cycle in the proportion of particles originating from each origin box for the PnB

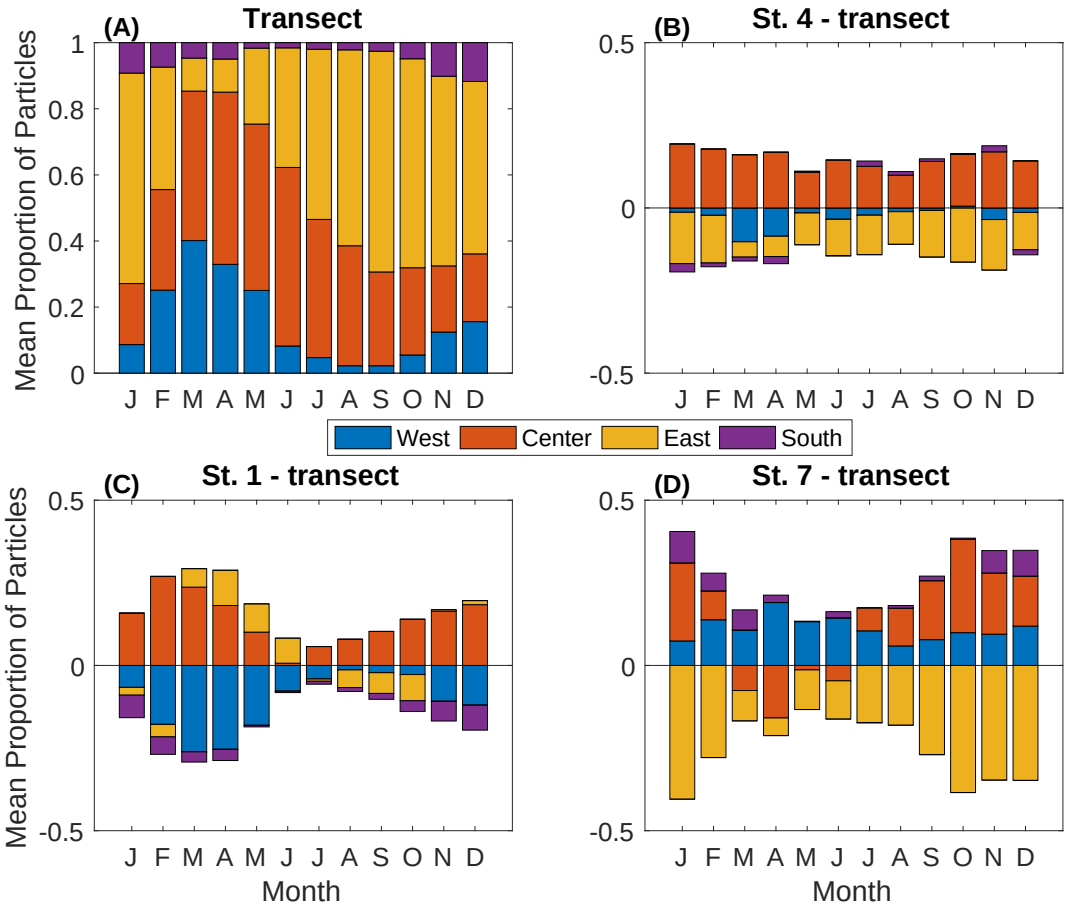

Figure 14. Mean annual cycles in the proportion of particles originating from each of the four origin boxes (see Figures 1 and 13) for (A) all release points on the PnB transect, and for the four to five release points closest to PnB stations (B) 4, (C) 1, and (D) 7 minus the transect mean annual cycle. The station-specific mean annual cycles are presented as differences relative to the entire transects mean annual cycle. The proportion of particles originating from the west (east) origin box serves as a proxy for the magnitude of advection of CCS (SCBight) source waters.

transect. The seasonal cycle in SBC source waters appeared to be tightly coupled to seasonal upwelling. Across the PnB transect, the proportion of particles from the West origin box (Figures 1 and 13), a proxy for the magnitude of advection of CCS sources waters, was highest in March and elevated (>20%) from February through May (Figure 14A). Conversely, advection of SCBight waters into the SBC as indicated by the proportion of particles originating from the East origin box was lowest in March and April and subsequently increased until reaching an annual maximum in September (Figure 14A), as expected (Harms and Winant, 1998). Relatively few particles reached the PnB transect from the South origin box.

Seasonal cycles in the source waters of the northern- and southern-most portions of the SBC deviated substantially from that observed for the PnB transect as a whole (Figure 14C-D). From March through June, the proportion of particles originating from the CCS at the southern-most release points (closest to PnB station 7) was >10% higher than observed for the transect, and was >5% higher throughout the remainder of the year (Figure 14D). The opposite pattern was observed at the release points closest to PnB station 1 in the northern SBC (Figure 14C). This cumulatively represents a ~20-40% difference in CCS source water advection between PnB stations 1 and 7 from March through June (Figure 14). These differences are associated with 1-2 $\mu g\ L^{-1}$ higher monthly mean diatom biomarker pigment concentrations at PnB station 7 relative to station 1 from March through September, and smaller but significantly different picophytoplankton concentrations at station 7 relative to station 1 (Figure 7). Shorter-term studies have previously documented advection of harmful diatom blooms associated with elevated domoic acid concentrations from the southern CCS into the southwestern SBC during the late summer and fall (Anderson et al., 2009). Our results suggest this phenomenon may be a consistent source of elevated phytoplankton concentrations in the SBC during the late summer

and fall. Consistently higher dinoflagellate concentrations in the northern SBC (station 1) relative to the southern SBC (Figure 7) are also linked to consistently higher advection of SCBight source waters (Figure 14). Overall, these findings support our hypothesis that the relative magnitude of advection of CCS and SCBight source waters into the SBC plays a substantial role in driving spatial variations in SBC PG dynamics on seasonal and interannual time scales.

On interannual to decadal time scales, we hypothesized that NPGO-driven variations in the advection of SCBight source waters into the SBC (Di Lorenzo et al., 2008; Di Lorenzo et al., 2013) provide favorable conditions and/or seed dinoflagellate populations enabling the anomalous decadal dinoflagellate blooms observed above to develop (Figures 5, 8, 9, 11, and 12). We test this hypothesis using the simulated source water determinations for the entire PnB transect by comparing monthly anomalies in the proportion of particles advected from each origin box with the observed NPGO and dinoflagellate biomarker pigment dynamics (Figure 15). Anomalously high advection of SCBight source waters was found almost every month from 2004 to late 2007 (Figure 15A), coupled with a warm phase of the NPGO (Figure 15B) and consistently high dinoflagellate concentrations (Figure 15C). Conversely, from late 2007 through 2013, the cold phase of the NPGO was coupled with only sporadic observations of anomalously high advection of SCBight source waters and dinoflagellate concentrations.

Consideration of the monthly dynamics leading to the dinoflagellate bloom in early 2006 further supports this hypothesis. An anomalously large red tide dominated by the Perid-containing *Lingulodinium polyedrum* (Zapata et al., 2012) was observed over a large extent of the nearshore SCBight from March through September in 2005 (Santoro et al., 2010). Monthly mean Perid concentrations in the SBC rose from 0.22 μg L^{-1} in August 2005 to ~0.7 μg L^{-1} in

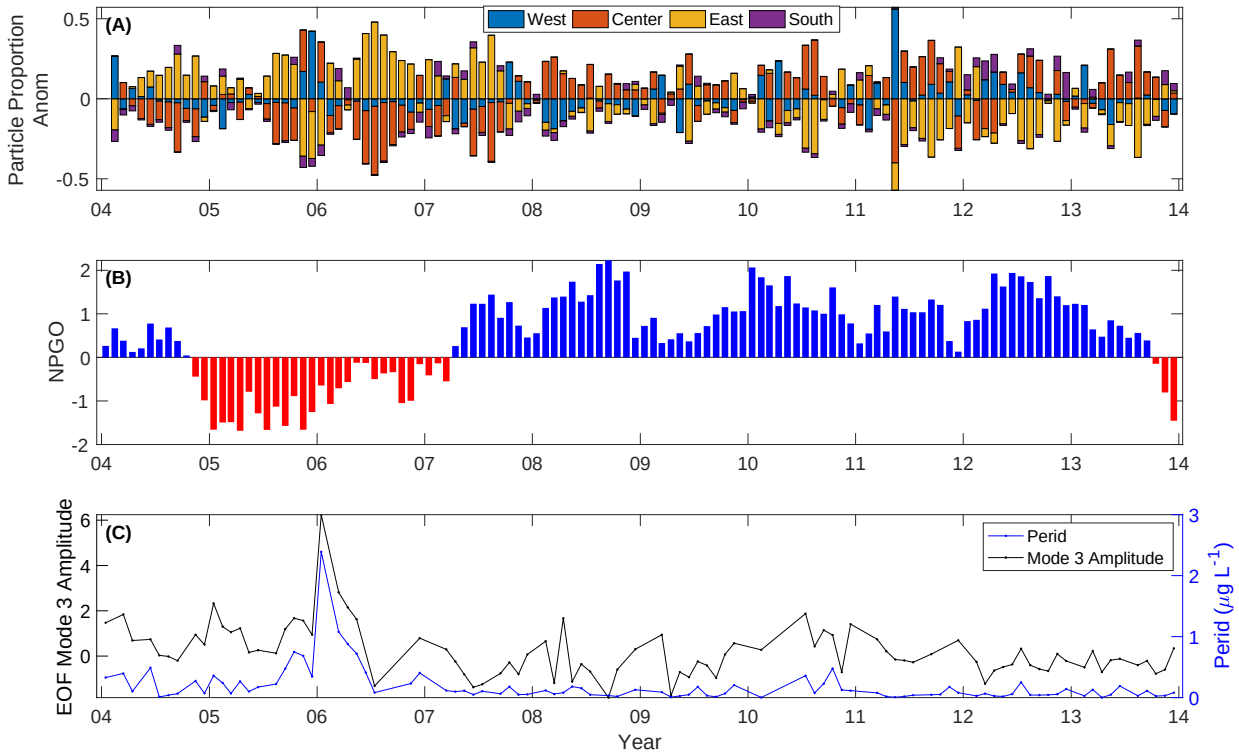

Figure 15. Time series of (A) anomalies in the proportion of particles advected from each of the four origin boxes determined by the ROMS particle tracking model (see Figures 1, 13, and 14) for the entire PnB transect, (B) the North Pacific Gyre Oscillation index, and (C) monthly mean Perid concentrations and EOF Mode 3 amplitudes.

October and November 2005, coinciding with anomalously high advection of SCBight source waters from July to October 2005 (Figure 15C). This pattern was interrupted by a highly anomalous intrusion of CCS source waters from November 2005 to January 2006 (Figure 15A), interpreted here as an introduction of nutrient-rich waters to the SBC that enabled growth and accumulation of dinoflagellates (monthly mean Perid concentration of 2.39 µg L^{-1} in January, 2006; see Figure 15C). While other factors must align to allow for the accumulation of dinoflagellates in SBC surface waters, these results highlight the importance of advection in driving the anomalous decadal dinoflagellate blooms observed above (Figure 5).

Altogether, the ROMS backwards particle tracking simulations provide strong evidence that our Eulerian observations of seasonal to multi-decadal PG dynamics in the SBC are

impacted by variability in the advection of different source waters into the SBC. Seasonally elevated diatom biomarker pigment concentrations in the southwestern SBC were associated with seasonally elevated advection of CCS source waters, while decadal dinoflagellate blooms were associated with anomalously high advection of SCBight source waters linked to the warm phase of the NPGO. However, it remains unknown whether these contrasting source waters harbor "seed" populations of PGs that are primed for or in the midst of blooming, or if local SBC PG populations are favored by the oceanographic properties of the source waters. Further targeted studies focusing on synoptic perspectives of PG bloom events in addition to genetic studies of SBC PG populations relative to those found in the CCS and SCBight may resolve this question. Regardless, seasonal to interannual variability in source water origins should be accounted for in studies of long-term PG dynamics, particularly in oceanographic transition zones like the SBC.

4.4. Oceanographic and climate forcing of PG dynamics in the SBC

Wind-driven upwelling has long been recognized as the dominant forcing of seasonal to interannual variations in phytoplankton biomass, productivity, and community composition in the SBC, CCS, and SCBight (Goodman et al., 1984; Venrick, 2002; Anderson et al., 2008; Barth et al., 2020; Fischer et al., 2020). The focus of most studies to date has been on the seasonal "succession" (though this is not equivalent to succession as traditionally defined by ecologists; see Barber and Hiscock, 2006) of the phytoplankton community from a diatom-dominated community during periods of significant spring upwelling to a dinoflagellate-dominated community as the water column becomes more stratified following the relaxation of upwelling in summer and fall (Margalef, 1978; Goodman et al., 1984; Anderson et al., 2008;

Barth et al., 2020; Fischer et al., 2020). Due to limitations of methods relying on visual identification of PGs, the seasonal dynamics of nano- and pico-phytoplankton groups are often not considered, although long-term epifluorescence microscopy observations have documented some seasonal and interannual variations in pico- and nano-phytoplankton groups (Taylor et al., 2015; Caron et al., 2017). Here we discuss the complimentary view of the responses of the phytoplankton community, particularly pico- and nano-phytoplankton groups, to seasonal upwelling and climate forcings provided by the biomarker pigment time series presented above in the context of past studies reliant on microscopic PG observations in upwelling systems.

The EOF analysis of biomarker pigments and oceanographic observations above (Figures 10 and 11) shows the progressive responses of different PGs to seasonal upwelling. While the diatoms tend to reach the highest overall cell densities (Anderson et al., 2006; Venrick, 2012; Taylor et al., 2015; Caron et al., 2017) and pigment biomass (Anderson et al., 2008; Figure 6) in response to upwelling, the loading pattern and monthly mean amplitudes of EOF Mode 1 show that the typical "first responders" to seasonal upwelling in the SBC are the chlorophytes and prymnesiophytes (Figures 6 and 10). On average, the annual peak in diatom pigment biomass occurs in April or May, after the initial peak in chlorophyte and prymnesiophyte pigment biomass in March (Figures 6 and 10). These results are consistent with previous observations in the SBC and SCBight showing high winter-time abundances of nano-phytoplankton and annual maxima in prymnesiophyte abundances in the early spring (Taylor et al., 2015; Caron et al., 2017). Similarly, some pico- and nano-phytoplankton respond positively to elevated nutrient concentrations in the broader CCS as well as in the equatorial Pacific upwelling zone (Barber and Hiscock, 2006; Taylor and Landry, 2018). Reduced top-down regulation of diatoms relative to smaller-sized PGs likely explains the tendency for diatoms to accumulate more biomass than

prymnesiophytes and chlorophytes in response to favorable growth conditions (see Taylor and Landry, 2018 for a detailed discussion), though further study is needed to confirm this hypothesis in the SBC. Regardless, these observations suggest that assumptions of a neutral or negative response of all pico- and/or nano-phytoplankton to elevated nutrient concentrations often employed in marine ecosystem models should be revisited, as suggested previously (Barber and Hiscock, 2006; Taylor and Landry, 2018).

Interestingly, we did not find an obvious pattern of phytoplankton community "succession" from a diatom bloom in spring/summer to a period of elevated dinoflagellate concentrations in summer/fall as might be predicted in some interpretations of Margalef's mandala (Margalef, 1978; Figures 6 and 10). The large multi-decadal variations in Perid concentrations combined with the poor performance of the bio-optical model when predicting low Perid concentrations (Figure 4; Supp. Figures S6 and S7) may have obscured underlying seasonal dinoflagellate variations. However, the mean annual cycles of Fuco and Perid at PnB station 1 on the mainland shelf showed signs of the dynamics predicted by Margalef's mandala (Supp. Figure S11), and publicly available microscopy observations at the nearby Stearns Wharf, Santa Barbara, CA often show a seasonal increase in cell abundances of some dinoflagellates beginning in the late spring and early summer and extending into the early fall (Supp. Figure S12). These findings support previous suggestions of a decoupling of PG dynamics on the inner continental shelf (water depths < ~30 to 40 m) from those observed further offshore in the SBC, SCBight, and central CCS (Lucas et al., 2011; Goodman et al., 2012; Schulien et al., 2017), and more broadly demonstrate the importance of pairing near-shore marine ecosystem monitoring programs (e.g., SCCOOS) with offshore observations. In agreement with previous studies (Gregorio and Pieper, 2000; Fischer et al., 2020), the covariance of temperature and salinity

1177 loadings in opposition to the Perid loading in EOF Mode 3 (Figures 10 and 11) suggest that
1178 sporadic winter-time precipitation and freshwater discharge events are likely a more prominent
1179 forcing of dinoflagellate blooms in the broader SBC region than seasonal relaxations of
1180 upwelling winds.

1181 Interannual variations in the oceanographic manifestations of seasonal upwelling are
1182 largely dictated by climate forcings, most notably the ENSO (Bograd and Lynn, 2001; Venrick,
1183 2012; Jacox et al., 2016), PDO (Mantua et al., 1997; Jacox et al., 2014), and NPGO (Di Lorenzo
1184 et al., 2008; Di Lorenzo et al., 2013; Jacox et al., 2014). El Niño events drive an anomalously
1185 stratified water column and deepening of the nutricline in the SCBight and CCS, which generally
1186 leads to anomalously low phytoplankton biomass (Bograd and Lynn, 2001; Venrick, 2012). The
1187 impacts of the ENSO on SBC PG dynamics are demonstrated above (Figures 8, 9, 11, 12). The
1188 two strongest El Niño events (1997-98 and 2015-16) over our 22 years of observations were
1189 accompanied by anomalously low pigment biomass for 4 of the 5 PGs investigated (all except
1190 picophytoplankton; Figures 8 and 9). The conditional averaging of EOF amplitudes by the two
1191 indices of the ENSO confirm that La Niña events favor enhanced upwelling and the associated
1192 responses of the chlorophytes, prymnesiophytes, and diatoms in EOF Modes 1, 2 and 4, while El
1193 Niño events favor higher picophytoplankton concentrations (Figure 12). Dinoflagellate
1194 concentrations as indicated by Perid and EOF Mode 3 also appear higher during La Niña events
1195 despite a lack of clear associations with the oceanographic signatures of upwelling (Figure 12).

1196 Although a 22-year time series only offers a limited view of decadal processes, our
1197 observations provide a glimpse into low-frequency PG variations governed by the NPGO and
1198 PDO. The dominant decadal pattern observed in the PG data set was the anomalous
1199 dinoflagellate blooms associated with the warm phase of the NPGO and the cold phase of the

PDO (Figures 8, 9, 11, and 12). Anomalously high dinoflagellate abundances have been recently observed in association with the warm phase of the NPGO on the inner shelf of Central California (Barth et al., 2020; Fischer et al., 2020), suggesting this association may hold for a significant portion of the CCS and SCBight. In conjunction with the remote forcing of the NPGO, these studies have proposed a combination of increased freshwater discharge events (also corroborated by our analysis; Figures 10 and 12) and increased water column stratification in driving these dinoflagellate anomalies (Barth et al., 2020; Fischer et al., 2020). Figures 14 and 15 above suggest that enhanced advection of SCBight source waters plays an important role in driving these blooms in the SBC, though it is unclear if this phenomenon would extend north of Point Conception.

The NPGO and PDO are also expected to impact PG responses to seasonal upwelling (Mantua et al., 1997; Di Lorenzo et al., 2008; Chenillat et al., 2012; Di Lorenzo et al., 2013). The cold phases of the NPGO and PDO apparently favored the upwelling responsive PGs identified above (diatoms, prymnesiophytes, and chlorophytes; see Figure 12). Interestingly, EOF Modes 2 and 4 resolved two independent (by definition of the EOF analysis) diatom bloom states. While both were favored by the cold phases of the ENSO, NPGO, and PDO, EOF Mode 2 showed an annual maximum in May and was significantly impacted by the ENSO (Figure 12; $r = 0.19$, $p = 0.008$), but EOF Mode 4 showed an annual maximum in June and was significantly impacted by the NPGO (Figure 12; $r = 0.16$, $p = 0.03$). The mechanisms driving these differences are not clear and require further exploration, though both the ENSO and NPGO are thought to impact the timing of seasonal upwelling in the broader CCS and this may partially explain these results (Bograd et al., 2009; Chenillat et al., 2012). These results suggest that extreme NPGO and ENSO

events, along with the associated impacts on oceanographic and other forcings, may lead to unique realizations of seasonal diatom bloom dynamics.

Taken together, our results reveal the seasonal to multi-decadal oceanographic and climate forcings of the dominant PGs in and around the SBC. In addition to diatoms, several smaller-sized PGs accumulate pigment biomass in response to seasonal upwelling in the SBC. All PGs that exhibit seasonal variability associated with upwelling are impacted by interannual variations in seasonal upwelling linked to forcing by the ENSO, NPGO, and PDO. Seasonal variability in source water advection drives pronounced cross-SBC variability in annual PG cycles, particularly in the magnitude of diatom blooms, while decadal dinoflagellate blooms in the SBC are linked to the NPGO, freshwater discharge, and multi-decadal changes in regional advection patterns. Future research is required to determine the roles of top-down forcings in shaping the dynamics of phytoplankton communities in the SBC, as well as to clarify the underlying mechanisms linking decadal dinoflagellate blooms to anomalous regional advection patterns.

Acknowledgements

We thank the past and present members of the Plumes and Blooms team for their many years of dedicated sampling and analysis efforts, and acknowledge helpful conversations with Debora Iglesias-Rodriguez, Libe Washburn, Chris Gotschalk, Mark Brzezinski, and Sasha Kramer. We also thank three anonymous peer reviewers for helpful feedback on the manuscript. Plumes and Blooms is funded by the National Aeronautics and Space Administration (NASA; NNX11AL94G), and ship time for the data presented here was provided by NASA and the National Oceanic and Atmospheric Administration (NOAA) Channel Islands National Marine

Sanctuary. Additional support of this work and of DC was provided by the NASA Biodiversity and Ecological Forecasting program (Grant NNX14AR62A), the Bureau of Ocean and Energy Management Ecosystem Studies program (BOEM award MC15AC00006) and NOAA in support of the Santa Barbara Channel Marine Biodiversity Observation Network, the NASA PACE Science Team (Grant 80NSSC20M0226), and the NSF Santa Barbara Coastal Long Term Ecological Research site (Grant OCE 1232779). DC was also funded in part by a NASA Earth and Space Science Fellowship (Grant NNX16AO44HS02).

Declaration of Competing Interests

The authors declare no competing or conflicts of interest.

References

Allen WE. 1942. Occurrences of "red water" near San Diego. *Science* **96**(2499): 471–471.

Anderson CR, Brzezinski MA, Washburn L, Kudela R. 2006. Circulation and environmental conditions during a toxigenic Pseudo-nitzschia australis bloom in the Santa Barbara Channel, California. *Marine Ecology Progress Series* **327**: 119–133.

Anderson CR, Siegel DA, Brzezinski MA, Guillocheau N. 2008. Controls on temporal patterns in phytoplankton community structure in the Santa Barbara Channel, California. *Journal of Geophysical Research: Oceans* **113**(C4).

Anderson, CR, Siegel, DA, Kudela, RM, Brzezinski, MA. 2009. Empirical models of toxigenic Pseudo-nitzschia blooms: potential use as a remote detection tool in the Santa Barbara Channel. *Harmful Algae*, **8**(3): 478-492.

Barber R, Hiscock M. 2006. A rising tide lifts all phytoplankton: Growth response of other phytoplankton taxa in diatom-dominated blooms. *Global Biogeochemical Cycles* **20**(4). Wiley Online Library.

Barrón RK, Siegel DA, Guillocheau N. 2014. Evaluating the importance of phytoplankton community structure to the optical properties of the Santa Barbara Channel, California. *Limnology and oceanography* **59**(3): 927–946. Wiley Online Library.

1274 Barth A, Walter RK, Robbins I, Pasulka A. 2020. Seasonal and interannual variability of
1275 phytoplankton abundance and community composition on the Central Coast of
1276 California. *Marine Ecology Progress Series* **637**: 29–43.

1277 Beers J. 1986. Organisms and the food web. *Plankton dynamics of the southern California Bight*
1278 **15**: 84–175. Wiley Online Library.

1279 Behrenfeld MJ, Boss ES. 2018. Student's tutorial on bloom hypotheses in the context of
1280 phytoplankton annual cycles. *Global change biology* **24**(1): 55–77. Wiley Online Library.

1281 Bialonski S, Caron DA, Schloen J, Feudel U, Kantz H, Moorthi SD. 2016. Phytoplankton
1282 dynamics in the Southern California Bight indicate a complex mixture of transport and
1283 biology. *Journal of Plankton Research* **38**(4): 1077–1091.

1284 Bograd SJ, Lynn RJ. 2001. Physical-biological coupling in the California Current during the
1285 1997–99 El Niño-La Niña cycle. *Geophysical Research Letters* **28**(2): 275–278. Wiley
1286 Online Library.

1287 Bograd SJ, Schroeder I, Sarkar N, Qiu X, Sydeman WJ, Schwing FB. 2009. Phenology of coastal
1288 upwelling in the California Current. *Geophysical Research Letters* **36**(1).

1289 Bond NA, Cronin MF, Freeland H, Mantua N. 2015. Causes and impacts of the 2014 warm
1290 anomaly in the NE Pacific. *Geophysical Research Letters* **42**(9): 3414–3420.

1291 Brzezinski MA, Washburn L. 2011. Phytoplankton primary productivity in the Santa Barbara
1292 Channel: Effects of wind-driven upwelling and mesoscale eddies. *Journal of Geophysical*
1293 *Research: Oceans* **116**(C12).

1294 Caron DA, Connell PE, Schaffner RA, Schnetzer A, Fuhrman JA, Countway PD, Kim DY. 2017.
1295 Planktonic food web structure at a coastal time-series site: I. Partitioning of microbial
1296 abundances and carbon biomass. *Deep Sea Research Part I: Oceanographic Research*
1297 *Papers* **121**: 14–29. Elsevier.

1298 Carr SD, Capet XJ, McWilliams JC, Pennington JT, Chavez FP. 2008. The influence of diel
1299 vertical migration on zooplankton transport and recruitment in an upwelling region:
1300 Estimates from a coupled behavioral-physical model. *Fisheries Oceanography* **17**(1): 1–
1301 15. Wiley Online Library.

1302 Catlett D, Siegel DA, Guillocheau N. 2020a. Plumes and Blooms: Curated oceanographic and
1303 phytoplankton pigment observations ver 1. Environmental Data
1304 Initiative. https://doi.org/10.6073/pasta/f88ee1dc32b8785fe6ce57d80722e78c.

1305 Catlett D, Siegel DA, Carlson CA, Matson PG, Wear EK, Iglesias-Rodriguez MD. 2020b.
1306 Integrating high-throughput sequencing observations into remotely sensible
1307 phytoplankton functional type determinations. Ocean Sciences Meeting 2020. AGU.

Catlett D, Siegel DA. 2018. Phytoplankton pigment communities can be modeled using unique relationships with spectral absorption signatures in a dynamic coastal environment. *Journal of Geophysical Research: Oceans* **123**(1): 246–264.

Chase A, Boss E, Cetinić I, Slade W. 2017. Estimation of phytoplankton accessory pigments from hyperspectral reflectance spectra: toward a global algorithm. *Journal of Geophysical Research: Oceans* **122**(12): 9725–9743. Wiley Online Library.

Chavez FP, Pennington JT, Castro CG, Ryan JP, Michisaki RP, Schlining B, Walz P, Buck KR, McFadyen A, Collins CA. 2002. Biological and chemical consequences of the 1997–1998 El Niño in central California waters. *Progress in Oceanography* **54**(1–4): 205–232.

Chenillat F, Rivière P, Capet X, Di Lorenzo E, Blanke B. 2012. North Pacific Gyre Oscillation modulates seasonal timing and ecosystem functioning in the California Current upwelling system. *Geophysical Research Letters* **39**(1).

Chhak K, Di Lorenzo E. 2007. Decadal variations in the California Current upwelling cells. *Geophysical Research Letters* **34**(14).

Countway PD, Caron DA. 2006. Abundance and distribution of Ostreococcus sp. in the San Pedro Channel, California, as revealed by quantitative PCR. *Applied and Environmental Microbiology* **72**(4): 2496–2506.

Di Lorenzo E, Combes V, Keister JE, Strub PT, Thomas AC, Franks PJ, Ohman MD, Furtado JC, Bracco A, Bograd SJ. 2013. Synthesis of Pacific Ocean climate and ecosystem dynamics. *Oceanography* **26**(4): 68–81.

Di Lorenzo E, Schneider N, Cobb KM, Franks PJS, Chhak K, Miller AJ, McWilliams JC, Bograd SJ, Arango H, Curchitser E. 2008. North Pacific Gyre Oscillation links ocean climate and ecosystem change. *Geophysical Research Letters* **35**(8).

Dong C, Idica EY, McWilliams JC. 2009. Circulation and multiple-scale variability in the Southern California Bight. *Progress in Oceanography* **82**(3): 168–190. Elsevier.

Dong C, McWilliams JC, Hall A, Hughes M. 2011. Numerical simulation of a synoptic event in the Southern California Bight. *Journal of Geophysical Research: Oceans* **116**(C5). Wiley Online Library.

Dong, C., L. Renault, Y. Zhang, J, Ma, and Y. Cao, 2017: Expansion of West Coast Oceanographic Modeling Capability. US Department of the Interior, Bureau of Ocean Energy Management, Pacific. OCS Study BOEM 2017-055. 83 pp.

Fewings, M.R., Washburn, L. and Ohlmann, J.C., 2015. Coastal water circulation patterns around the northern Channel Islands and Point Conception, California. *Progress in Oceanography*, *138*, pp.283-304.

Field CB, Behrenfeld MJ, Randerson JT, Falkowski P. 1998. Primary production of the biosphere: integrating terrestrial and oceanic components. *Science* **281**(5374): 237–240.

Fischer AD, Hayashi K, McGaraghan A, Kudela RM. 2020. Return of the "age of dinoflagellates" in Monterey Bay: Drivers of dinoflagellate dominance examined using automated imaging flow cytometry and long-term time series analysis. *Limnology and Oceanography*. Wiley Online Library.

Goodman D, Eppley R, Reid F. 1984. Summer phytoplankton assemblages and their environmental correlates in the Southern California Bight. *Journal of Marine Research* **42**(4): 1019–1049. Sears Foundation for Marine Research.

Goodman J, Brzezinski MA, Halewood ER, Carlson CA. 2012. Sources of phytoplankton to the inner continental shelf in the Santa Barbara Channel inferred from cross-shelf gradients in biological, physical and chemical parameters. *Continental Shelf Research* **48**: 27–39.

Gregorio DE, Pieper RE. 2000. Investigations of red tides along the southern California coast. *Bulletin of the Southern California Academy of Sciences* **99**(3): 147–147.

Guidi L, Chaffron S, Bittner L, Eveillard D, Larhlimi A, Roux S, Darzi Y, Audic S, Berline L, Brum JR. 2016. Plankton networks driving carbon export in the oligotrophic ocean. *Nature* **532**(7600): 465.

Guillocheau, N, 2003. Beta-Correction Experiment Report. ICESS Internal document, UCSB, April 2003.

Hamed, KH, & Rao, AR. 1998. A modified Mann-Kendall trend test for autocorrelated data. *Journal of hydrology*, **204**(1-4), 182-196.

Harms S, Winant CD. 1998. Characteristic patterns of the circulation in the Santa Barbara Channel. *Journal of Geophysical Research: Oceans* **103**(C2): 3041–3065.

Henderikx Freitas F, Siegel DA, Maritorena S, Fields E. 2017. Satellite assessment of particulate matter and phytoplankton variations in the Santa Barbara Channel and its surrounding waters: R ole of surface waves. *Journal of Geophysical Research: Oceans* **122**(1): 355–371.

Higgins HW, Wright SW, Schluter L. 2011. Quantitative interpretation of chemotaxonomic pigment data. In: *Phytoplankton Pigments: Characterization, Chemotaxonomy, and Applications in Oceanography*. Cambridge University Press.

Hirata T, Hardman-Mountford N, Brewin R, Aiken J, Barlow R, Suzuki K, Isada T, Howell E, Hashioka T, Noguchi-Aita M. 2011. Synoptic relationships between surface Chlorophyll-a and diagnostic pigments specific to phytoplankton functional types. *Biogeosciences* **8**(2): 311–327. Copernicus Publications.

Hooker SB, Thomas CS, Van Heukelem L, Russ ME, Ras J, Claustre H, Clementson L, Canuti E, Berthon J-F, Perl J. 2010. The fourth SeaWiFS HPLC analysis round-Robin experiment (SeaHARRE-4). NASA Technical Memorandum.

Jacox MG, Hazen EL, Zaba KD, Rudnick DL, Edwards CA, Moore AM, Bograd SJ. 2016. Impacts of the 2015–2016 El Niño on the California Current System: Early assessment and comparison to past events. *Geophysical Research Letters* **43**(13): 7072–7080.

Jacox MG, Moore AM, Edwards CA, Fiechter J. 2014. Spatially resolved upwelling in the California Current System and its connections to climate variability. *Geophysical Research Letters* **41**(9): 3189–3196.

Jeffrey SW, Wright SW, Zapata M. 2011. Microalgal classes and their signature pigments. In: *Phytoplankton Pigments: Characterization, Chemotaxonomy, and Applications in Oceanography*. Cambridge University Press.

Johnson KS, Petty RL, Thomsen J. 1985. Flow-injection analysis for seawater micronutrients. *Advances in Chemistry* **209**. ACS Publications.

Kahru M, Kudela RM, Manzano-Sarabia M, Mitchell BG. 2012. Trends in the surface chlorophyll of the California Current: Merging data from multiple ocean color satellites. *Deep Sea Research Part II: Topical Studies in Oceanography* **77**: 89–98. Elsevier.

Kramer SJ, Siegel, DA. 2019. How can phytoplankton pigments be best used to characterize surface ocean phytoplankton groups for ocean color remote sensing algorithms?. *Journal of Geophysical Research: Oceans*, **124**(11), 7557-7574. Wiley Online Library.

Krause JW, Brzezinski MA, Siegel DA, Thunell RC. 2013. Biogenic silica standing stock and export in the Santa Barbara Channel ecosystem. *Journal of Geophysical Research: Oceans* **118**(2): 736–749. Wiley Online Library.

Latasa M, Bidigare RR. 1998. A comparison of phytoplankton populations of the Arabian Sea during the Spring Intermonsoon and Southwest Monsoon of 1995 as described by HPLC-analyzed pigments. *Deep Sea Research Part II: Topical Studies in Oceanography* **45**(10–11): 2133–2170.

Lin Y, Cassar N, Marchetti A, Moreno C, Ducklow H, Li Z. 2017. Specific eukaryotic plankton are good predictors of net community production in the Western Antarctic Peninsula. *Scientific reports* **7**(1): 1–11. Nature Publishing Group.

Lombard F, Boss E, Waite AM, Vogt M, Uitz J, Stemmann L, Sosik HM, Schulz J, Romagnan J-B, Picheral M. 2019. Globally consistent quantitative observations of planktonic ecosystems. *Frontiers in Marine Science* **6**: 196. Frontiers.

Lucas AJ, Dupont CL, Tai V, Largier JL, Palenik B, Franks PJ. 2011. The green ribbon: Multiscale physical control of phytoplankton productivity and community structure over a narrow continental shelf. *Limnology and Oceanography* **56**(2): 611–626.

Mackey M, Mackey D, Higgins H, Wright S. 1996. CHEMTAX-a program for estimating class abundances from chemical markers: application to HPLC measurements of phytoplankton. *Marine Ecology Progress Series* **144**: 265–283.

1419 Mantua NJ, Hare S. 2002. Pacific-Decadal Oscillation (PDO). *Encyclopedia of global*
1420 *environmental change* **1**: 592–594.

1421 Mantua NJ, Hare SR, Zhang Y, Wallace JM, Francis RC. 1997. A Pacific interdecadal climate
1422 oscillation with impacts on salmon production. *Bulletin of the american Meteorological*
1423 *Society* **78**(6): 1069–1080.

1424 Margalef R. 1978. Life-forms of phytoplankton as survival alternatives in an unstable
1425 environment. *Oceanologica acta* **1**(4): 493–509. Gauthier-Villars.

1426 Matson PG, Washburn L, Fields EA, Gotschalk C, Ladd TM, Siegel DA, Welch ZS, Iglesias-
1427 Rodriguez MD. 2019. Formation, development, and propagation of a rare coastal
1428 coccolithophore bloom. *Journal of Geophysical Research: Oceans* **124**(5): 3298–3316.

1429 McDougall, T.J. and P.M. Barker, 2011: Getting started with TEOS-10 and the Gibbs Seawater
1430 (GSW) Oceanographic Toolbox, 28pp., SCOR/IAPSO WG127, ISBN 978-0-646-55621-
1431 5.
1432
1433 McPhee-Shaw EE, Siegel DA, Washburn L, Brzezinski MA, Jones JL, Leydecker A, Melack J.
1434 2007. Mechanisms for nutrient delivery to the inner shelf: Observations from the Santa
1435 Barbara Channel. *Limnology and Oceanography* **52**(5): 1748–1766.

1436 Melton C, Washburn L, Gotschalk C. 2009. Wind relaxations and poleward flow events in a
1437 coastal upwelling system on the central California coast. *Journal of Geophysical*
1438 *Research: Oceans* **114**(C11).

1439 Mitarai S, Siegel DA, Watson J, Dong C, McWilliams J. 2009. Quantifying connectivity in the
1440 coastal ocean with application to the Southern California Bight. *Journal of Geophysical*
1441 *Research: Oceans* **114**(C10). Wiley Online Library.

1442 Mitchell BG. 1990. Algorithms for determining the absorption coefficient for aquatic particulates
1443 using the quantitative filter technique. Ocean optics X **1302**: 137–148. International
1444 Society for Optics and Photonics.

1445 Needham DM, Fuhrman JA. 2016. Pronounced daily succession of phytoplankton, archaea and
1446 bacteria following a spring bloom. *Nature Microbiology* **1**(4): 16005.

1447 Nygaard K, Tobiesen A. 1993. Bacterivory in algae: a survival strategy during nutrient
1448 limitation. *Limnology and Oceanography* **38**(2): 273–279. Wiley Online Library.

1449 Ohlmann JC, Mitarai S. 2010. Lagrangian assessment of simulated surface current dispersion in
1450 the coastal ocean. *Geophysical Research Letters* **37**(17). Wiley Online Library.

1451 Otero MP, Siegel DA. 2004. Spatial and temporal characteristics of sediment plumes and
1452 phytoplankton blooms in the Santa Barbara Channel. *Deep Sea Research Part II: Topical*
1453 *Studies in Oceanography* **51**(10–11): 1129–1149.

1454 Palenik B. 2000. Picophytoplankton seasonal cycle at the SIO pier, La Jolla, California. *Journal*
1455 *of Phycology* **36**: 53–53. Wiley Online Library.

1456 Reid F, Stewart E, Eppley R, Goodman D. 1978. Spatial distribution of phytoplankton species in
1457 chlorophyll maximum layers off southern California. *Limnology and Oceanography*
1458 **23**(2): 219–226. Wiley Online Library.

1459 Roesler C, Stramski D, D'Sa E, Röttgers R, Reynolds RA. 2018. Spectrophotometric
1460 measurements of particulate absorption using filter pads. *Washington, DC: IOCCG*.

1461 Santoro AE, Nidzieko NJ, van Dijken GL, Arrigo KR, Boehma AB. 2010. Contrasting spring
1462 and summer phytoplankton dynamics in the nearshore Southern California Bight.
1463 *Limnology and Oceanography* **55**(1): 264–278.

1464 Schulien, JA, Peacock, MB, Hayashi, K, Raimondi, P, Kudela, RM. 2017. Phytoplankton and
1465 microbial abundance and bloom dynamics in the upwelling shadow of Monterey Bay,
1466 California, from 2006 to 2013. *Marine Ecology Progress Series*, **572**: 43-56.
1467
1468 Shipe R, Passow U, Brzezinski M, Graham W, Pak D, Siegel D, Alldredge A. 2002. Effects of
1469 the 1997–98 El Nino on seasonal variations in suspended and sinking particles in the
1470 Santa Barbara basin. *Progress in Oceanography* **54**(1–4): 105–127. Elsevier.

1471 Siegel DA, Behrenfeld MJ, Maritorena S, McClain CR, Antoine D, Bailey SW, Bontempi PS,
1472 Boss ES, Dierssen HM, Doney SC. 2013. Regional to global assessments of
1473 phytoplankton dynamics from the SeaWiFS mission. *Remote Sensing of Environment*
1474 **135**: 77–91.

1475 Simons RD, Nishimoto MM, Washburn L, Brown KS, Siegel DA. 2015. Linking kinematic
1476 characteristics and high concentrations of small pelagic fish in a coastal mesoscale eddy.
1477 *Deep Sea Research Part I: Oceanographic Research Papers* **100**: 34–47.

1478 Simons RD, Siegel DA, Brown KS. 2013. Model sensitivity and robustness in the estimation of
1479 larval transport: a study of particle tracking parameters. *Journal of Marine Systems* **119**:
1480 19–29. Elsevier.

1481 Smayda TJ, Trainer VL. 2010. Dinoflagellate blooms in upwelling systems: Seeding, variability,
1482 and contrasts with diatom bloom behaviour. *Progress in Oceanography* **85**(1–2): 92–107.

1483 Taylor AG, Landry MR. 2018. Phytoplankton biomass and size structure across trophic gradients
1484 in the southern California Current and adjacent ocean ecosystems. *Marine Ecology*
1485 *Progress Series* **592**: 1–17.

1486 Taylor AG, Landry MR, Selph KE, Wokuluk JJ. 2015. Temporal and spatial patterns of
1487 microbial community biomass and composition in the Southern California Current
1488 Ecosystem. *Deep Sea Research Part II: Topical Studies in Oceanography* **112**: 117–128.

1489 Thomson RE, Emery WJ. 2014. *Data Analysis Methods in Physical Oceanography*. Newnes.

Trees CC, Kennicutt II MC, Brooks JM. 1985. Errors associated with the standard fluorimetric determination of chlorophylls and phaeopigments. *Marine Chemistry* **17**(1): 1–12. Elsevier.

Uitz J, Claustre H, Morel A, Hooker SB. 2006. Vertical distribution of phytoplankton communities in open ocean: An assessment based on surface chlorophyll. *Journal of Geophysical Research: Oceans* **111**(C8).

U.S. Integrated Ocean Observing System. 2013. Manual for Real-Time Quality Control of In-situ Temperature and Salinity Data: A Guide to Quality Control and Quality Assurance of In-situ Temperature and Salinity Observations.

Van Boekel J, Stefels W. 1993. Production of DMS from dissolved DMSP in axenic cultures of the marine phytoplankton species Phaeocystis sp. *Marine Ecology Progress Series* **97**: 11–18.

Van Heukelem L, Thomas CS. 2001. Computer-assisted high-performance liquid chromatography method development with applications to the isolation and analysis of phytoplankton pigments. *Journal of Chromatography A* **910**(1): 31–49.

de Vargas C, Aubry M-P, Probert I, Young J. 2007. Origin and evolution of coccolithophores: from coastal hunters to oceanic farmers. In: *Evolution of Primary Producers in the Sea*. Elsevier. p. 251–285.

Venrick EL. 1998. The phytoplankton of the Santa Barbara Basin: patterns of chlorophyll and species structure and their relationships with those of surrounding stations. *California Cooperative Oceanic Fisheries Investigations Report*: 124–132. California Cooperative Oceanic Fisheries Investigations.

Venrick EL. 2002. Floral patterns in the California Current System off southern California: 1990-1996. *Journal of Marine Research* **60**(1): 171–189.

Venrick EL. 2012. Phytoplankton in the California Current system off southern California: Changes in a changing environment. *Progress in Oceanography* **104**: 46–58. Elsevier.

Vidussi F, Claustre H, Manca BB, Luchetta A, Marty J. 2001. Phytoplankton pigment distribution in relation to upper thermocline circulation in the eastern Mediterranean Sea during winter. *Journal of Geophysical Research: Oceans* **106**(C9): 19939–19956. Wiley Online Library.

Warrick JA, Mertes LA, Washburn L, Siegel DA. 2004. A conceptual model for river water and sediment dispersal in the Santa Barbara Channel, California. *Continental Shelf Research* **24**(17): 2029–2043. Elsevier.

Wear EK, Carlson CA, James AK, Brzezinski MA, Windecker LA, Nelson CE. 2015. Synchronous shifts in dissolved organic carbon bioavailability and bacterial community responses over the course of an upwelling-driven phytoplankton bloom. *Limnology and Oceanography* **60**(2): 657–677.

Winant CD, Dever EP, Hendershott MC. 2003. Characteristic patterns of shelf circulation at the boundary between central and southern California. *Journal of Geophysical Research: Oceans* **108**(C2). Wiley Online Library.

Wolter K, Timlin MS. 1993. Monitoring ENSO in COADS with a Seasonally Adjusted Principal. 1993. Proc. of the 17th Climate Diagnostics Workshop, Norman, OK, NOAA/NMC/CAC, NSSL, Oklahoma Clim. Survey, CIMMS and the School of Meteor., Univ. of Oklahoma, 52.

Worden AZ, Nolan JK, Palenik B. 2004. Assessing the dynamics and ecology of marine picophytoplankton: the importance of the eukaryotic component. *Limnology and oceanography* **49**(1): 168–179.

Zapata M, Fraga S, Rodríguez F, Garrido JL. 2012. Pigment-based chloroplast types in dinoflagellates. *Marine Ecology Progress Series* **465**: 33–52.